JOURNAL OF COMPUTATIONAL PHYSICS **138,** 939–980 (1997)
ARTICLE NO. CP975847

The Development of a Free Surface Capturing Approach for Multidimensional Free Surface Flows in Closed Containers

F. J. Kelecy and R. H. Pletcher

Department of Mechanical Engineering, Iowa State University, Ames, Iowa 50014
E-mail: pletcher@iastate.edu

Received September 9, 1997

A new surface-capturing method is developed for numerically simulating viscous free surface flows in partially filled containers. The method is based on the idea that the flow of two immiscible fluids within a closed container is governed by the equations of motion for an incompressible, viscous, nonhomogeneous (variable density) fluid. By computing the flow fields in both the liquid and gas regions in a consistent manner, the free surface can be captured as a discontinuity in the density field, thereby eliminating the need for special free surface tracking procedures. The numerical algorithm is developed using a conservative, implicit, finite volume discretization of the equations of motion. The algorithm incorporates the artificial compressibility method in conjunction with a dual time-stepping strategy to maintain a divergence-free velocity field. A slope-limited, high-order MUSCL scheme is adopted for approximating the inviscid flux terms, while the viscous fluxes are centrally differenced. The capabilities of the surface capturing method are demonstrated by calculating solutions to several two- and three-dimensional problems.

Key Words: free surface; incompressible; two-fluid.

1. INTRODUCTION

The motion of fluids within partially filled containers has been the subject of much study by scientists and engineers due, in large part, to its importance in many practical applications. For example, civil engineers and seismologists have actively studied the effects of earthquake-induced fluid motions on oil tanks and water towers [8]. In recent years, aerospace engineers have been concerned with the effect of fluid sloshing within propellant tanks on the stability of aircraft, rockets, and

0021-9991/97 $25.00

satellites [1]. All of these applications seek container designs which minimize the amplitude of fluid forces over a gain range of operating conditions. Typically, this is accomplished by either modifying the natural frequency of the fluid-container system or by introducing baffling devices to damp the fluid motion.

Despite the power and capacity available in present day computers, the numerical simulation of fluid motion within partially filled containers is still a challenging problem. One of the principal reasons for this is that the flow field is usually three-dimensional and unsteady. Numerical solutions of such flows typically require a large number of time steps and, as a result, can consume enormous amounts of computer memory, CPU time, and disk storage. Another difficulty which arises in free surface flows is the modeling of the free surface itself. In the present context, a free surface can be defined as the interface between the liquid and a secondary fluid (usually a gas) which occupies the remaining space within the container. Since the position of the free surface is not known a priori, it must be determined as part of the flow field solution. The free surface motion may also be influenced by various interfacial phenomena, such as surface tension and mass transfer.

Numerical approaches for handling free surface problems can be grouped into three broad categories: surface fitting methods, surface tracking methods, and surface capturing methods. Surface fitting methods solve for the flow within the liquid region only, the free surface being placed at the boundary of the computational domain. The motion of the free surface is accounted for by a coordinate transformation which maps the moving, body-fitted coordinate system in physical space to a fixed, uniformly spaced coordinate system in computational space. If the free surface becomes highly distorted, a new mesh may have to be generated in order to prevent both grid singularities and highly skewed grid point distributions.

The surface tracking and surface capturing methods avoid the grid-related problems associated with surface fitting methods by employing a grid which is fixed relative to the container and by defining the location of the liquid and gas regions relative to the fixed grid. This practice requires an enlargement of the computational domain to encompass the entire container, since the free surface can potentially occupy any position within the fixed grid. The principal difference between the surface tracking and surface capturing schemes is the manner in which the location of the liquid is identified. Surface tracking methods typically discretize the computational domain into nonoverlapping cells which are then ''flagged,'' depending on whether the cell contains all liquid, all gas, or the free surface. The governing equations are then solved in the liquid and free surface cells only. The cells must be reflagged at each time step to reflect the new free surface configuration. Surface capturing methods, on the other hand, solve for the flow field within both the liquid and the gas cells simultaneously. The location of the free surface is ''captured'' as a discontinuity in the density field, thus eliminating the need for tracking procedures. This idea is similar in spirit to the ''shock capturing'' approach, which has been applied extensively to simulations of compressible flows with shock waves.

One of the first numerical schemes to employ the surface tracking idea was the marker and cell (MAC) method of Harlow and Welch [11]. In the MAC method, the free surface location was identified by placing discrete, massless ''marker particles'' in the liquid and convecting them according to the instantaneous velocity field.

The flow field solution was then updated within the liquid using an explicit scheme. A significant improvement to the MAC method was later developed by Hirt and Nichols [14]. Called the volume of fluid (VOF) method, it identified the location of the free surface by using a scalar function $F(x, y, z, t)$ to represent the fraction of liquid contained in a cell. This function was updated using a transport equation to model the convection of F. As with the MAC method, only the flow field within the liquid and free surface cells was computed.

Several surface capturing-type schemes were developed by various researchers, including Spalding [32], Ramshaw and Trapp [26], and Maxwell and Spalding [23]. Ramshaw and Trapp used a nonconservative form of the momentum and energy equations, along with a transport equation for density to model the sloshing of water and steam in a rectangular container. Their approach employed a modified donor–acceptor differencing technique to resolve the phase interface (free surface). Both Spalding and Maxwell employed the SIMPLE method for incompressible flows in conjunction with a particle tracking procedure to determine the location of the free surface. Unlike the MAC method, however, their approach obtained flow field solutions in both the liquid and the gas simultaneously. This method was later modified by Jun and Spalding [18] to incorporate a simple transport equation to update the density field. Special upwinding and property evaluation procedures were used to minimize the diffusion of the density interface. Several two-dimensional computations were presented to demonstrate the effectiveness of their approach.

Several methods have appeared in recent years which address some of the shortcomings of previous surface tracking and surface capturing schemes. Unverdi and Tryggvason [36] developed a front-tracking scheme which solved for the liquid and gas flow fields on a stationary grid and represented the free surface using a separate unstructured grid. Since the free surface grid could deform in an arbitrary manner, their algorithm allowed for some restructuring of this grid during the course of a given calculation. Results for two- and three-dimensional simulations of bubble motion were reported. Sussman *et al.* [33] presented an approach based on the level set method. This method, which is similar to the approach of Jun and Spalding [18], used the zero level set of a smooth function to identify the free surface. Results for several two-dimensional cases involving the motion of air bubbles in water and falling water drops in air were shown.

This paper describes a new surface capturing approach which has been developed by the authors for computing two- and three-dimensional free surface flows within closed containers. In contrast to previous methods, the present approach makes use of the artificial compressibility method [7] in conjunction with the governing equations for a viscous, incompressible, variable density flow to develop a conservative, fully coupled numerical algorithm. To demonstrate the present surface capturing method, results are presented for the two-dimensional "broken dam" problem, the two-dimensional Rayleigh–Taylor instability, and the three-dimensional "broken dam" problem.

2. MATHEMATICAL MODEL

In the free surface capturing approach, a flow field solution is sought within both the liquid and gas regions of the computational domain. A mathematical model of

this two-fluid system must therefore be able to simulate the physics in both regions in a consistent manner.

Given the complexity of the general free surface flow problem, it is necessary to introduce some simplifying assumptions in order to make the resulting formulation tractable. The present work assumes that the two fluids are immiscible, with both the density and viscosity constant within each fluid, and that the flow field is incompressible, laminar, and isothermal. For convenience in the discussions below, the fluid properties in the liquid and gas regions will be denoted respectively by the subscripts 1 and 2. It should be noted that while the primary fluid is usually a liquid and the secondary fluid is a gas, the present formulation is applicable to any fluid combination (e.g., liquid–liquid), as long as the foregoing assumptions are satisfied. Finally, for all of the problems considered here, surface tension forces and interfacial mass transfer are neglected.

2.1. *Governing Equations*

The mathematical model of the two-fluid system is based upon the system of partial differential equations which govern the motion of a viscous, incompressible, variable density (nonhomogeneous) fluid. These equations can be written in conservation form as follows:

- Conservation of mass,

$$\frac{\partial \rho}{\partial t} + \nabla \cdot \rho \mathbf{V} = 0; \tag{1}$$

- Conservation of momentum,

$$\frac{\partial \rho \mathbf{V}}{\partial t} + \nabla \cdot (\rho \mathbf{V}\mathbf{V} - \overline{\overline{\mathbf{T}}}) = \rho \mathbf{B}; \tag{2}$$

- Incompressibility constraint,

$$\nabla \cdot \mathbf{V} = 0. \tag{3}$$

In the above, ρ is the mass density, $\mathbf{V} = u\hat{\imath} + v\hat{\jmath} + w\hat{k}$ is the velocity vector, $\mathbf{B} = B_x\hat{\imath} + B_y\hat{\jmath} + B_z\hat{k}$ is the body force acceleration vector, and $\overline{\overline{\mathbf{T}}}$ is the stress tensor for an incompressible fluid,

$$\overline{\overline{\mathbf{T}}} = \mu[\nabla \mathbf{V} + (\nabla \mathbf{V})^T] - \overline{\overline{\mathbf{I}}} p, \tag{4}$$

where μ is the dynamic viscosity, p is the thermodynamic pressure, and $\overline{\overline{\mathbf{I}}}$ denotes the unit dyad.

While Eqs. (1)–(3) appear unusual at first glance because of the presence of an equation for density, they do in fact constitute a solvable system of equations. Detailed discussions of the mathematical properties of these equations have been presented by Simon [31] and Antontsev *et al.* [2]. Similar formulations have also been considered by Kataoka [19], Unverdi and Tryggvason [36], and Sussman *et al.*

[33]. It should be noted that Eqs. (1)–(3) do not account for any interfacial effects (e.g., surface tension).

To complete the specification of the mathematical problem, Eqs. (1)–(3) must be supplemented with appropriate boundary and initial conditions. Since the fluid domain is confined to a closed container, all physical boundaries will be impermeable walls. The initial conditions will, of course, depend on the particular problem under consideration.

2.2. *Free Surface Modeling*

At the interface between two immiscible fluids, experimental observations show that fluid properties are not discontinuous, but instead vary continuously within a narrow transition zone [10]. Since the width of this transition zone is typically on the order of 10^{-9} m, it is reasonable to adopt the idealization that the interface is a singular surface (or collection of surfaces) which can be described mathematically by an equation (or set of equations) of the form

$$f_i(x, y, z, t) = 0. \tag{5}$$

From an analysis of the kinematics of the interface, it can be shown that the motion of the surface $f_i(x, y, z, t)$ is governed by [30]

$$\frac{\partial f_i}{\partial t} + \mathbf{V} \cdot \nabla f_i = 0. \tag{6}$$

This equation is often referred to as the kinematic boundary condition.

If it is assumed that the fluid interface can be modeled as a singular surface then, in the absence of viscosity, Eqs. (1) and (2) reduce to a system of conservation laws which are hyperbolic in both space and time. Using the condition that the free surface is a material interface (and, hence, moves with the fluid), it can be shown that the inviscid system admits discontinuous solutions wherein both the density and tangential velocity may undergo discrete jumps at the free surface [17].

Due to the diffusive effects of viscosity and the molecular mixing which occurs at the interface, solutions to the viscous equations will, in fact, be continuous. However, since the length scales associated with property variations across discontinuities are usually much smaller than the characteristic length of the system under study, one cannot, as a practical matter, resolve such variations numerically. Consequently, the free surface still appears as a discontinuity in a numerical solution to the viscous equations.

Following the arguments given above, the present work assumes that the system of equations for nonhomogeneous, incompressible flow can be used to numerically compute free surface flows by ''capturing'' the free surface as a contact discontinuity in the density field. Specifically, it is asserted that the numerical solution of Eqs. (1)–(3) for a system containing one or more free surfaces will converge (in the inviscid limit) to the correct weak solution. Since the free surface is ''captured'' as a discontinuity in the density field, the need for special procedures to track the free

surface is eliminated. It should be noted that the concept of obtaining weak solutions to Eqs. (1)–(3) for the purpose of modeling two-fluid flows is not new. In particular, Kataoka [19] developed a theoretical framework for this idea in the context of two phase flows. In this work, the differential equations governing the motion of a general two phase system were derived based on the use of generalized functions (or distributions). It was then shown that if interfacial phenomena were neglected, the equations for two phase flow had the same form as those for single phase flow. However, the derivatives for the two phase model were defined in the sense of a distribution. A detailed discussion of these ideas can be found in Kataoka's article.

2.3. *The Artificial Compressibility Method*

In the present formulation, it is assumed that the flow field is incompressible, as reflected by the inclusion of Eq. (3). If density and viscosity of the two fluids are identical then Eqs. (1)–(3) reduce to the incompressible Navier–Stokes equations. It is reasonable, therefore, to examine numerical approaches which have been used successfully for the incompressible Navier–Stokes equations, and we apply them (with suitable modifications) to the surface capturing model.

The approach adopted in the present work for solving the two-fluid, incompressible system is based on the artificial compressibility method of Chorin [7]. The artificial compressibility method augments Eq. (3) with a fictitious time derivative of pressure as follows:

$$\frac{1}{\beta}\frac{\partial p}{\partial \tau} + \nabla \cdot \mathbf{V} = 0. \tag{7}$$

Here, β is a constant (with units of pressure) and τ is a parameter known as the pseudo-time. Originally, the artificial compressibility method was thought to be applicable only to steady flow problems. For such problems, the entire time dependence was fictitious, with the correct steady state solution being approached asymptotically in pseudo-time as suggested above. More recently, however, several investigators have introduced time-accurate algorithms in which both the physical time t and the pseudo-time τ are marched [29]. In this case, the solution at a given physical time level is approached asymptotically as a steady state solution in pseudo-time. This type of algorithm, which is often called the dual time-stepping procedure, is employed in the present work as a means of computing time-accurate solutions using the artificial compressibility approach.

3. NUMERICAL FORMULATION

The numerical approach for solving the governing equations presented above is based on the finite volume method. The finite volume method discretizes the computational domain as a system of nonoverlapping control volumes or cells. The relevant partial differential equations are then integrated over each cell, yielding a system of integral equations. Applying specific spatial and temporal discretization techniques transforms these integral equations into a set of algebraic equations,

where the unknowns represent spatial averages of the dependent variables for a given control volume.

In order to apply the finite volume method to the two-fluid system, Eqs. (1), (2), and (7) are first cast into the integral conservation law forms

$$\frac{d}{dt}\int_{\Omega} \mathbf{U}\, d\Omega + \oint_S \mathbf{F}\cdot\hat{n}\, dS = \int_{\Omega} \mathbf{B}\, d\Omega, \tag{8}$$

$$\frac{1}{\beta}\frac{d}{dt}\int_{\Omega} p\, d\Omega + \oint_S \mathbf{V}\cdot\hat{n}\, dS = 0, \tag{9}$$

where Ω is the cell volume, S is the bounding surface, and column vectors $\mathbf{U}$, $\mathbf{F}$, and $\mathbf{B}$ are defined as

$$\mathbf{U} = \begin{bmatrix} \rho \\ \rho u \\ \rho v \\ \rho w \end{bmatrix} \tag{10}$$

$$\mathbf{F} = \mathbf{F}_{\text{inv}} - \mathbf{F}_{\text{vis}} \tag{11}$$

$$\mathbf{F}_{\text{inv}} = \begin{bmatrix} \rho\mathbf{V} \\ \rho\mathbf{V}u + p\hat{\imath} \\ \rho\mathbf{V}v + p\hat{\jmath} \\ \rho\mathbf{V}w + p\hat{k} \end{bmatrix} \tag{12}$$

$$\mathbf{F}_{\text{vis}} = \begin{bmatrix} 0 \\ \mu\left(\dfrac{\partial\mathbf{V}}{\partial x} + \nabla u\right) \\ \mu\left(\dfrac{\partial\mathbf{V}}{\partial y} + \nabla v\right) \\ \mu\left(\dfrac{\partial\mathbf{V}}{\partial z} + \nabla w\right) \end{bmatrix} \tag{13}$$

$$\mathbf{B} = \begin{bmatrix} 0 \\ B_x \\ By \\ B_z \end{bmatrix}. \tag{14}$$

Spatial discretizations of the foregoing integral equations are now constructed to transform the integral equation for a given control volume into an ordinary differential equation:

$$\frac{d}{dt}(\mathbf{U}\Omega) + \sum_{l=1}^{6} (\mathbf{F}\cdot\mathbf{S})_l = \mathbf{B}\Omega \tag{15}$$

$$\frac{d}{d\tau}(P\Omega) + \sum_{l=1}^{6} (\mathbf{V}\cdot\mathbf{S})_l = 0. \tag{16}$$

In the above, $P = p/\beta$ and $\mathbf{S}_l$ is the surface area vector associated with face l of the control volume.

Using the trapezoidal scheme to advance Eq. (15) in physical time yields

$$\frac{\Omega}{\Delta t}(\mathbf{U}^{n+1} - \mathbf{U}^n) + \theta\left[\sum_{l=1}^{6} (\mathbf{F}\cdot\mathbf{S})_l - \mathbf{B}\Omega\right]^{n+1} + (1-\theta)\left[\sum_{l=1}^{6} (\mathbf{F}\cdot\mathbf{S})_l - \mathbf{B}\Omega\right]^{n} = 0. \tag{17}$$

Since the pseudo-compressibility equation does not require second-order accuracy in pseudo-time, the Euler implicit form of the trapezoidal scheme ($\theta = 1$) is preferred due to its more favorable stability. Equation (16) can thus be written as

$$\frac{\Omega}{\Delta\tau}(P^{m+1} - P^m) + \left[\sum_{l=1}^{6} (\mathbf{V}\cdot\mathbf{S})_l\right]^{m+1} = 0, \tag{18}$$

where m is the pseudo-time index.

Equations (17) and (18) can now be combined by observing that quantities at the $m + 1$ time level must approach the solution at the next physical time level $n + 1$ in the limit as m approaches infinity. Thus, the index $n + 1$ in Eq. (17) can be replaced by the index $m + 1$, giving

$$\frac{\Omega}{\Delta t}(\mathbf{U}^{m+1} - \mathbf{U}^n) + \theta\left[\sum_{l=1}^{6} (\mathbf{F}\cdot\mathbf{S})_l - \mathbf{B}\Omega\right]^{m+1} + (1-\theta)\left[\sum_{l=1}^{6} (\mathbf{F}\cdot\mathbf{S})_l - \mathbf{B}\Omega\right]^{n} = 0. \tag{19}$$

Equations (18) and (19) can now be written as the single column vector equation

$$\frac{\Omega}{\Delta\tau}([\mathbf{I}] - [\mathbf{I}_0])\,\delta\mathbf{U} + \frac{\Omega}{\Delta t}[\mathbf{I}_0](\delta\mathbf{U} + \mathbf{U}^m - \mathbf{U}^n) + [\mathbf{I}_\theta]\left[\sum_{l=1}^{6} (\mathbf{F}\cdot\mathbf{S})_l - \mathbf{B}\Omega\right]^{m+1} + ([\mathbf{I}] - [\mathbf{I}_\theta])\left[\sum_{l=1}^{6} (\mathbf{F}\cdot\mathbf{S})_l - \mathbf{B}\Omega\right]^{n} = 0, \tag{20}$$

where $\delta\mathbf{U} \equiv \mathbf{U}^{m+1} - \mathbf{U}^m$, the diagonal matrices are given by

$$[\mathbf{I}] = \mathrm{diag}(1, 1, 1, 1, 1) \tag{21}$$

$$[\mathbf{I}_0] = \mathrm{diag}(1, 1, 1, 1, 0) \tag{22}$$

$$[\mathbf{I}_\theta] = \mathrm{diag}(\theta, \theta, \theta, \theta, 1) \tag{23}$$

and $\mathbf{U}$, $\mathbf{F}$, and $\mathbf{B}$ have been redefined as

$$\mathbf{U} = \begin{bmatrix} \rho \\ \rho u \\ \rho v \\ \rho w \\ P \end{bmatrix} \tag{24}$$

$$\mathbf{F} = \mathbf{F}_{\text{inv}} - \mathbf{F}_{\text{vis}} \tag{25}$$

$$\mathbf{F}_{\text{inv}} = \begin{bmatrix} \rho \mathbf{V} \\ \rho \mathbf{V} u + \beta P \hat{\imath} \\ \rho \mathbf{V} v + \beta P \hat{\jmath} \\ \rho \mathbf{V} w + \beta P \hat{k} \\ \mathbf{V} \end{bmatrix} \tag{26}$$

$$\mathbf{F}_{\text{vis}} = \begin{bmatrix} 0 \\ \mu \left(\dfrac{\partial \mathbf{V}}{\partial x} + \nabla u \right) \\ \mu \left(\dfrac{\partial \mathbf{V}}{\partial y} + \nabla v \right) \\ \mu \dfrac{\partial \mathbf{V}}{\partial z} + \nabla w \Big) \\ 0 \end{bmatrix} \tag{27}$$

$$\mathbf{B} = \begin{bmatrix} 0 \\ B_x \\ By \\ B_z \\ 0 \end{bmatrix}. \tag{28}$$

This formulation is similar to the implicit scheme described by Pan and Chakravarthy [25] for incompressible flows. In the present case, however, the pseudo-time marching process is used instead of a relaxed Newton-iteration approach.

3.1. *Flux Evaluation*

The formulation of the inviscid fluxes is based on the upwind-biased MUSCL scheme of van Leer [37]. This scheme, which was originally developed for the compressible Euler equations, has been applied to a wide variety of problems by various authors, including unsteady, incompressible flows [25]. In the present work, the MUSCL scheme is used in conjunction with Roe's approximate Riemann solver

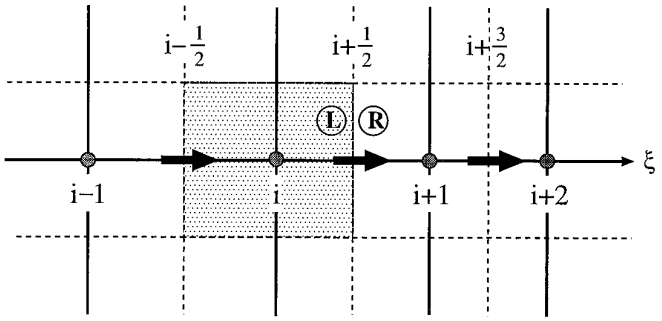

FIG. 1. Illustration of flux evaluation for upwind-biased MUSCL scheme.

[28] to construct a numerical flux, as shown in Fig. 1. The essential ideas behind this formulation will be discussed below.

Roe's scheme is based on a local, linear wave decomposition of the inviscid flux difference across a cell face. The numerical flux arising from Roe's scheme can be expressed in the following manner: Let $[\mathbf{A}_{\text{inv}}]$ denote the Jacobian of the inviscid flux vector, $\mathbf{F}_{\text{inv}} \equiv \mathbf{F}_{\text{inv}} \cdot \mathbf{S}$,

$$[\mathbf{A}_{\text{inv}}] \equiv \frac{\partial \mathbf{F}_{\text{inv}}}{\partial \mathbf{U}}. \tag{29}$$

Also, let $[\tilde{\mathbf{A}}_{\text{inv}}]$ be defined as the matrix $[\mathbf{A}_{\text{inv}}]$, evaluated at an average state $\tilde{\mathbf{U}} = \tilde{\mathbf{U}}(\mathbf{U}^L, \mathbf{U}^R)$, where L and R denote the left and right states, as shown in Fig. 1.

The numerical flux $\hat{\mathbf{F}}_{\text{inv}}$ can then be written as

$$\hat{\mathbf{F}}_{\text{inv}} = \tfrac{1}{2}\,[\mathbf{F}_{\text{inv}}(\mathbf{U}^R) + \mathbf{F}_{\text{inv}}(\mathbf{U}^L) - [\mathbf{D}_i](\mathbf{U}^R - \mathbf{U}^L)], \tag{30}$$

where

$$[\mathbf{D}_i] = [\tilde{\mathbf{T}}][|\tilde{\Lambda}|][\tilde{\mathbf{T}}]^{-1}. \tag{31}$$

In the above $[\tilde{\mathbf{T}}]$ is a matrix whose columns are the right eigenvectors of $[\tilde{\mathbf{A}}_{\text{inv}}]$ and $[|\tilde{\Lambda}|]$ is a diagonal matrix consisting of the absolute values of the eigenvalues of $[\tilde{\mathbf{A}}_{\text{inv}}]$. For the inviscid flux vector given by Eq. (26), the Jacobian matrix $[\mathbf{A}_{\text{inv}}]$ and its associated eigenvalues and eigenvectors (and, hence, $[|\tilde{\Lambda}|]$, $[\tilde{\mathbf{T}}]$, and $[\tilde{\mathbf{T}}]^{-1}$) can be derived in a straightforward manner (see Appendices A and B).

For the two-fluid system, the appropriate Roe average is obtained by computing $\tilde{\mathbf{U}}$ as follows:

$$\tilde{\mathbf{U}} = \begin{bmatrix} \tilde{\rho} \\ \tilde{\rho}\tilde{u} \\ \tilde{\rho}\tilde{v} \\ \tilde{\rho}\tilde{w} \\ \tilde{P} \end{bmatrix} \tag{32}$$

$$\tilde{\rho} = \chi \rho^L \tag{33}$$

$$\tilde{u} = \frac{u^L + \chi u^R}{1 + \chi}, \tilde{v} = \frac{v^L + \chi v^R}{1 + \chi}, \tilde{w} = \frac{w^L + \chi w^R}{1 + \chi} \tag{34}$$

$$\tilde{P} = \tfrac{1}{2}(P^L + P^R) \tag{35}$$

$$\chi = \sqrt{\rho^R / \rho^L}. \tag{36}$$

The first-order form of Roe's scheme assumes a piecewise constant profile of $\mathbf{U}$ within each cell. For example, at cell face $i + \frac{1}{2}$,

$$\mathbf{U}^L_{i+1/2} = \mathbf{U}_i \tag{37}$$

$$\mathbf{U}^R_{i+1/2} = \mathbf{U}_{i+1}. \tag{38}$$

In order to achieve a spatial accuracy higher than first order, van Leer [37] observed that one can simply replace the piecewise constant profiles with higher order interpolations of $\mathbf{U}$ at the cell faces. The upwind-biased MUSCL scheme uses this idea to compute the numerical flux in the following manner:

1. Define high order upwind and downwind profiles of $\mathbf{U}$ at a given cell face.
2. Interpolate (or extrapolate) to obtain $\mathbf{U}^L$ using the upwind profile and $\mathbf{U}^R$ using the downwind profile.
3. Compute the numerical flux using an approximate Riemann solver (e.g., Roe's scheme).

A set of general interpolants developed by van Leer [37] can be defined for cell face $i + \frac{1}{2}$ as

$$\mathbf{U}^L_{i+1/2} = \mathbf{U} + \tfrac{1}{4}[(1 - \kappa)(\mathbf{U}_i - \mathbf{U}_{i-1}) + (1 + \kappa)(\mathbf{U}_{i+1} - \mathbf{U})] \tag{39}$$

$$\mathbf{U}^R_{i+1/2} = \mathbf{U}_{i+1} - \tfrac{1}{4}[(1 - \kappa)(\mathbf{U}_{i+2} - \mathbf{U}_{i+1}) + (1 + \kappa)(\mathbf{U}_{i+1} - \mathbf{U}_i)]. \tag{40}$$

The parameter κ in Eqs. (39) and (40) defines the order and type of interpolant. Some examples include the second-order upwind interpolant ($\kappa = -1$) and a third-order interpolant ($\kappa = \frac{1}{2}$) corresponding to the QUICK scheme of Leonard [21].

It is well known that higher order methods can give rise to spurious oscillations in the solution near discontinuities [12]. To control these oscillations, the present MUSCL scheme makes use of the following limiter functions:

$$(U^l)^L_{i+1/2} = U^l + \tfrac{1}{4}[(1 - \kappa)(\Phi^l)^R_{i-1/2}(U^l_i - U^l_{i-1}) + (1 + \kappa)(\Phi^l)^L_{i+1/2}(U^l_{i+1} - U^l_i)] \tag{41}$$

$$(U^l)^R_{i+1/2} = U^l_{i+1} - \tfrac{1}{4}[(1 - \kappa)(\Phi^l)^L_{i+3/2}(U^l_{i+2} - U^l_{i+1}) + (1 + \kappa)(\Phi^l)^R_{i+1/2}(U^l_{i+1} - U^l_i)]. \tag{42}$$

In the above, U^l denotes the lth component of the solution vector $\mathbf{U}$, and $(\Phi^l)^L_{i+1/2}$ and $(\Phi^l)^R_{i+1/2}$ are limiter functions which are defined as

TABLE I
Limiter Functions Applicable to the TVD MUSCL Scheme

Name	Limiter function
Minmod	$\Phi(r) = \max[0, \min(1, r)]$
Van Leer	$\Phi(r) = (r + \lvert r\rvert)/(1 + r)$
Compressive minmod[a]	$\Phi(r) = \max[0, \min(1, \omega r)]$
Superbee	$\Phi(r) = \max[0, \min(2r, 1), \min(r, 2)]$
MUSCL	$\Phi(r) = \max[0, \min(2, 2r, (1 + r)/2)]$

$$(\Phi^l)^L_{i+1/2} = \Phi((r^l)^L_{i+1/2}) \tag{43}$$

$$(\Phi^l)^R_{i+1/2} = \Phi((r^l)^R_{i+1/2}), \tag{44}$$

where

$$(r^l)^L_{i+1/2} = \frac{U^l - U^l_{i-1}}{U^l_{i+1} - U^l} \tag{45}$$

$$(r^l)^L_{i+1/2} = \frac{U^l_{i+2} - U^l_{i+1}}{U^l_{i+1} - U^l}. \tag{46}$$

The mathematical properties of slope-limited MUSCL schemes can be developed from the theory of total variation diminishing (TVD) schemes for one-dimensional, linear conservation laws [12]. From this analysis, it is found that many of the standard TVD limiters are possible candidates for the limiter functions used in Eqs. (41) and (42). Some typical limiter functions are given in Table I.

For systems of equations, $\mathbf{U}^L$ and $\mathbf{U}^R$ can also be constructed by interpolating other variables at the cell face (such as the primitive variables or characteristic variables) and computing the corresponding conserved variables from the interpolated variables. In the present case, it is advantageous to employ the primitive variables, $\mathbf{Q}$, where

$$\mathbf{Q} = \begin{bmatrix} \rho \\ u \\ v \\ w \\ p \end{bmatrix}. \tag{47}$$

Choosing the primitive variables allows a highly compressive limiter to be applied to the density (to help minimize numerical diffusion at the interface), while less compressive limiters (even no limiting) can be applied separately to the velocity components and pressure.

The one-dimensional inviscid flux formulas developed above can be employed in two- and three-dimensional formulations by simply using analogous formulas for each coordinate direction. That is, the i index is simply replaced by the j and k indices in order to obtain the numerical flux in the η and ζ directions, respectively. This practice, however, assumes that information travels along waves which propagate in directions normal to the cell faces. While this assumption is clearly violated if the local velocity vectors are not oriented normal to a given cell face, good results have nonetheless been observed in practice [28].

The viscous fluxes are discretized using central difference approximations following the general formulation outlined in Ref. [38]. In the present case, the viscous flux vector $\mathbf{F}_{\text{vis}}$ is constructed directly at a given cell face. The viscosity required at the cell face is computed by linearly interpolating from neighbor main grid point values,

$$\mu_{i+1/2} = \tfrac{1}{2}(\mu + \mu_{i+1}). \tag{48}$$

It should be noted that since the viscosity is assumed to be uniform within each fluid, the numerical value of μ at a given point can be derived from knowledge of the density distribution as follows:
First, define a parameter α as

$$\alpha \equiv \frac{\rho - \rho_2}{\rho_1 - \rho_2}. \tag{49}$$

It can be seen that α is one in the liquid and zero in the gas. Accordingly, the viscosity can be computed from

$$\mu = \alpha\mu_1 + (1 - \alpha)\mu_2. \tag{50}$$

3.2. *Linearization*

The final step of the discretization process is to linearize the $m + 1$ pseudo-time level terms about pseudo-time level m. To begin, the total flux $\mathbf{F}^{m+1}$ is expanded in a Taylor series about m as

$$\mathbf{F}^{m+1} = \mathbf{F}^m + \left(\frac{\partial \mathbf{F}}{\partial \tau}\right)^m \Delta\tau + \mathcal{O}[(\Delta\tau)^2], \tag{51}$$

where $\mathcal{O}[(\Delta\tau)^2]$ denotes terms of order $(\Delta\tau)^2$ and higher. Following Beam and Warming [4], the higher order terms are neglected and a discrete approximation for the first derivative term is constructed. Before doing this, the flux is split into inviscid and viscous parts, $\mathbf{F}^{m+1} = \mathbf{F}_{\text{inv}}^{m+1} + \mathbf{F}_{\text{vis}}^{m+1}$, where

$$\mathbf{F}_{\text{inv}}^{m+1} = \mathbf{F}_{\text{inv}}^{m} + \left(\frac{\partial \mathbf{F}_{\text{inv}}}{\partial \tau}\right)^m \Delta\tau \tag{52}$$

$$\mathbf{F}_{\text{vis}}^{m+1} = \mathbf{F}_{\text{vis}}^{m} + \left(\frac{\partial \mathbf{F}_{\text{vis}}}{\partial \tau}\right)^{m} \Delta\tau. \tag{53}$$

The inviscid flux time derivative term in Eq. (52) is expanded using the chain rule

$$\left(\frac{\partial \mathbf{F}_{\text{inv}}}{\partial \tau}\right)^{m} = \left(\frac{\partial \mathbf{F}_{\text{inv}}}{\partial \mathbf{U}}\right)^{m} \frac{\partial \mathbf{U}}{\partial \tau}. \tag{54}$$

Using the numerical flux $\hat{\mathbf{F}}_{\text{inv}} = \mathbf{F}_{\text{inv}}(\mathbf{U}^L, \mathbf{U}^R)$ in this equation gives

$$\left(\frac{\partial \mathbf{F}_{\text{inv}}}{\partial \tau}\right)^{m} = \left(\frac{\partial \hat{\mathbf{F}}_{\text{inv}}}{\partial \mathbf{U}^L}\right)^{m} \frac{\partial \mathbf{U}^L}{\partial \tau} + \left(\frac{\partial \hat{\mathbf{F}}_{\text{inv}}}{\partial \mathbf{U}^R}\right)^{m} \frac{\partial \mathbf{U}^R}{\partial \tau}. \tag{55}$$

The pseudo-time derivatives of $\mathbf{U}^L$ and $\mathbf{U}^R$ are now approximated with finite differences:

$$\frac{\partial \mathbf{U}^L}{\partial \tau} \approx \frac{(\mathbf{U}^L)^{m+1} - (\mathbf{U}^L)^m}{\Delta\tau} = \frac{\delta \mathbf{U}^L}{\Delta\tau} \tag{56}$$

$$\frac{\partial \mathbf{U}^R}{\partial \tau} \approx \frac{(\mathbf{U}^R)^{m+1} - (\mathbf{U}^R)^m}{\Delta\tau} = \frac{\delta \mathbf{U}^R}{\Delta\tau}. \tag{57}$$

Inserting these approximations into Eq. (55) yields

$$\left(\frac{\partial \mathbf{F}_{\text{inv}}}{\partial \tau}\right)^{m} \approx \left(\frac{\partial \hat{\mathbf{F}}_{\text{inv}}}{\partial \mathbf{U}^L}\right)^{m} \frac{\delta \mathbf{U}^L}{\Delta\tau} + \left(\frac{\partial \hat{\mathbf{F}}_{\text{inv}}}{\partial \mathbf{U}^R}\right)^{m} \frac{\delta \mathbf{U}^R}{\Delta\tau}. \tag{58}$$

It should be noted that both $\delta\mathbf{U}^L$ and $\delta\mathbf{U}^R$ can be expressed in terms of $\delta\mathbf{U}$ at the main grid points using the interpolation functions described in the previous section.

The Jacobians of the numerical flux $\partial\hat{\mathbf{F}}_{\text{inv}}/\partial\mathbf{U}^L$ and $\partial\hat{\mathbf{F}}_{\text{inv}}/\partial\mathbf{U}^R$ can be derived from the definition of Roe's numerical flux, Eq. (30). Following Barth [3], the Jacobians are simplified by neglecting terms arising from the derivatives of $[\mathbf{D}_i]$ with respect to $\mathbf{U}^L$ and $\mathbf{U}^R$. The resulting simplified Jacobians can be written as

$$\frac{\partial \hat{\mathbf{F}}_{\text{inv}}}{\partial \mathbf{U}^L} \approx \tfrac{1}{2}\left[[\mathbf{A}_{\text{inv}}(\mathbf{U}^L)] + [\mathbf{D}_i]\right] \equiv [\mathbf{A}_i^+] \tag{59}$$

$$\frac{\partial \hat{\mathbf{F}}_{\text{inv}}}{\partial \mathbf{U}^R} \approx \tfrac{1}{2}\left[[\mathbf{A}_{\text{inv}}(\mathbf{U}^R)] - [\mathbf{D}_i]\right] \equiv [\mathbf{A}_i^-]. \tag{60}$$

Substituting the simplified Jacobians in Eq. (55) gives

$$\left(\frac{\partial \mathbf{F}_{\text{inv}}}{\partial \tau}\right)^{m} \approx \frac{1}{\Delta\tau}\left[[\mathbf{A}_i^+]\,\delta\mathbf{U}^L + [\mathbf{A}_i^-]\,\delta\mathbf{U}^R\right]. \tag{61}$$

Thus, the linearized inviscid flux becomes

$$\mathbf{F}_i^{m+1} \approx \mathbf{F}_i^m + [\mathbf{A}_i^+]\,\delta\mathbf{U}^L + [\mathbf{A}_i^-]\,\delta\mathbf{U}^R. \tag{62}$$

For compactness, a flux difference $\delta\mathbf{F}_{\text{inv}}$ is defined by

$$\delta\mathbf{F}_{\text{inv}} \equiv [\mathbf{A}_i^+]\,\delta\mathbf{U}^L + [\mathbf{A}_i^-]\,\delta\mathbf{U}^R \tag{63}$$

so that Eq. (62) can be written

$$\mathbf{F}_i^{m+1} \approx \mathbf{F}_i^m + \delta\mathbf{F}_{\text{inv}}. \tag{64}$$

The linearization of the viscous Jacobian can be carried out in a similar fashion, yielding an expression similar to Eq. (64) above:

$$\mathbf{F}_v^{m+1} \approx \mathbf{F}_v^m + \delta\mathbf{F}_{\text{vis}}. \tag{65}$$

However, the Jacobian matrices which appear in $\delta\mathbf{F}_{\text{vis}}$ will be relatively complex if derived in full. As a result, it is common to either employ a simplified form of $\delta\mathbf{F}_{\text{vis}}$ (see, for example, [29]), or to neglect it altogether. In the present work, the following simplified form of $\delta\mathbf{F}_{\text{vis}}$ is employed at cell face $i + 1/2$,

$$\delta\mathbf{F}_{\text{vis}} = [\mathbf{D}_v])\delta\mathbf{U}_{i+1} - \delta\mathbf{U}), \tag{66}$$

where the elements of matrix $[\mathbf{D}_v]$ involve the viscosity and geometric parameters (see [20] for additional details).

The linearization of the body force term is reasonably straightforward, the result being represented as

$$\mathbf{B}^{m+1} \approx \mathbf{B}^m + [\mathbf{G}]\,\delta\mathbf{U}, \tag{67}$$

where

$$[\mathbf{G}] \equiv \partial\mathbf{B}/\partial\mathbf{U}. \tag{68}$$

The specific form of $[\mathbf{G}]$ will depend on the body force terms involved. For example, if the body force is due to a constant gravitational acceleration oriented in the y direction ($\rho\mathbf{B} = \rho g_e \hat{\jmath}$), then

$$[\mathbf{G}] = \text{diag}(g_e, 0, 0, 0, 0). \tag{69}$$

If the foregoing linearizations are introduced into Eq. (20), the result can be written as

$$\frac{\Omega}{\Delta\tau}([\mathbf{I}] + [\mathbf{H}])\,\delta U + [I_\theta]\left[\sum_{l=1}^{6}(\delta\mathbf{F}_{\text{inv}} - \delta\mathbf{F}_{\text{vis}})_l\right]^m = -\mathbf{R}, \tag{70}$$

where

$$\mathbf{R} = \frac{\Omega}{\Delta t}[\mathbf{I}_0](\mathbf{U}^m - \mathbf{U}^n) + [\mathbf{I}_\theta]\left[\sum_{l=1}^{6}(\mathbf{F}\cdot\mathbf{S})_l - \mathbf{B}\Omega\right]^m + ([\mathbf{I}] - [\mathbf{I}_\theta])\left[\sum_{l=1}^{6}(\mathbf{F}\cdot\mathbf{S})_l - \mathbf{B}\Omega\right]^n \quad (71)$$

$$[\mathbf{H}] = \left(\frac{\Delta\tau}{\Delta t} - 1\right)[\mathbf{I}_0] - \Delta\tau[\mathbf{I}_\theta][\mathbf{G}]^m. \quad (72)$$

Notice that setting $\mathbf{R}$ equal to zero yields a second-order accurate discretization of Eq. (20) in both space and time for $\theta = \frac{1}{2}$. Therefore, as long as the solution converges in pseudo-time (i.e., $\delta\mathbf{U} \to 0$), the computed solution is unaffected by the approximations made on the left-hand side.

Applying Eq. (70) to all control volumes and introducing appropriate expressions for $\delta\mathbf{F}_{\text{inv}}$ and $\delta\mathbf{F}_{\text{vis}}$ yields a block system of algebraic equations for the unknowns $\delta\mathbf{U}$. The solution at the next time level is obtained by marching the solution in pseudo-time until a steady state condition is achieved. In order to promote the stability of the pseudo-time marching process, it is desirable to enhance the diagonal dominance of the system of equations. One way of doing this in the present case is to add pseudo-time derivative terms to the mass and momentum equations. Note that this does not affect the computed solution, since all pseudo-time derivatives should approach zero in the limit as $m \to \infty$. Adding pseudo-time derivatives to Eq. (70) results in the following modified form of the [**H**] matrix:

$$[\mathbf{H}] = \frac{\Delta\tau}{\Delta t}[\mathbf{I}_0] - \Delta\tau[\mathbf{I}_\theta][\mathbf{G}]. \quad (73)$$

Another method for enhancing diagonal dominance is to employ a local pseudo-time step for each cell. An expression for the local pseudo-time step can be derived using the maximum eigenvalue (or spectral radius) of the flux Jacobian [12]. Denoting the spectral radii associated with the three computational coordinate directions as σ^ξ, σ^η, and σ^ζ, the local pseudo-time step can be determined from

$$\Delta\tau = \text{CFL}\min\left(\frac{\Omega}{\sigma^\xi}, \frac{\Omega}{\sigma^\eta}, \frac{\Omega}{\sigma^\zeta}\right), \quad (74)$$

where CFL is a CFL number (typically of order one).

3.3. *Boundary Conditions*

Boundary conditions were incorporated into the numerical formulation by expressing $\delta\mathbf{U}$ at boundary grid points in terms of both user-prescribed boundary data and the solution at interior grid points. For example, at the constant ξ boundary $i = 1$, a boundary equation can be written as

$$\delta\mathbf{U}_i = [\mathbf{C}^b_{w1}]\,\delta\mathbf{U}_{i+1} + [\mathbf{C}^b_{w2}]\,\delta\mathbf{U}_{i+2} + \mathbf{C}^b_{w3}, \quad (75)$$

where $[\mathbf{C}^b_{w1}]$, $[\mathbf{C}^b_{w2}]$, and $\mathbf{C}^b_{w3}$ are boundary coefficients associated with the $i = 1$ boundary. If this equation is substituted into Eq. (70) for grid point $i = 2$ (with $\delta\mathbf{F}_{\text{inv}}$ and $\delta\mathbf{F}_{\text{vis}}$ expressed in terms of $\delta\mathbf{U}$), then all references to the solution at $i = 1$ are eliminated. Since all the flow problems considered in the present work involve the motion of fluids within impermeable containers, only one type of boundary condition arises in the mathematical formulation, namely the viscous, impermeable wall boundary condition. Thus, no slip conditions on the boundaries are imposed on the velocity components ($u = v = w = 0$), and a pressure boundary condition derived from the normal component of the vector momentum equation is evaluated at the wall. The wall value of the density is simply extrapolated from the interior.

3.4. *Solution Procedure*

From the definition of the inviscid numerical flux, it is seen that the use of a high-order interpolant for δU^L and $\delta\mathbf{U}^R$ results in a large bandwidth matrix operator. To reduce this bandwidth, it is common to employ first-order upwind interpolation for the left-hand side operator. Using this simplification of the left-hand side operator, Eq. (71) can now be written

$$\begin{aligned}\frac{\Omega}{\Delta\tau}([\mathbf{I}] + [\mathbf{H}])\,\delta\mathbf{U} + [\mathbf{I}_\theta]\{&[([\mathbf{A}_i^+] + [\mathbf{D}_v])_{i+1/2} - ([\mathbf{A}_i^-] - [\mathbf{D}_v])_{i-1/2} + ([\mathbf{A}_i^+] + [\mathbf{D}_v])_{j+1/2} \\ &- ([\mathbf{A}_i^-] - [\mathbf{D}_v])_{j-1/2} + ([\mathbf{A}_i^+] + [\mathbf{D}_v])_{k-1/2} - ([\mathbf{A}_i^-] - [\mathbf{D}_v])_{k-1/2}]\,\delta\mathbf{U} \\ &+ ([\mathbf{A}_i^-] - [\mathbf{D}_v])_{i+1/2}\,\delta\mathbf{U}_{i+1} - ([\mathbf{A}_i^+] + [\mathbf{D}_v])_{i-1/2}\,\delta\mathbf{U}_{i-1} + ([\mathbf{A}_i^-] \\ &- [\mathbf{D}_v])_{j+1/2}\,\delta\mathbf{U}_{j+1} - ([\mathbf{A}_i^+] + [\mathbf{D}_v])_{j-1/2}\,\delta\mathbf{U}_{j-1} + ([\mathbf{A}_i^-] \\ &- [\mathbf{D}_v])_{k+1/2}\,\delta U_{k+1} - ([\mathbf{A}_i^+] + [\mathbf{D}_v])_{k-1/2}\,\delta\mathbf{U}_{k-1}\} = -\mathbf{R}. \end{aligned} \tag{76}$$

By introducing boundary equations of the form given by Eq. (75), the discrete, linearized system can be cast into the following form:

$$\begin{aligned}\frac{\Omega}{\Delta\tau}([\mathbf{I}] + [\mathbf{H}])\,\delta\mathbf{U} + [\mathbf{C}_P]\,\delta\mathbf{U} + [\mathbf{C}_E]\,\delta\mathbf{U}_{i+1} + [\mathbf{C}_W]\,\delta\mathbf{U}_{i-1} + [\mathbf{C}_N]\,\delta\mathbf{U}_{j+1} \\ + [\mathbf{C}_S]\,\delta\mathbf{U}_{j-1} + [\mathbf{C}_F]\,\delta\mathbf{U}_{k+1} + [\mathbf{C}_B]\,\delta\mathbf{U}_{k-1} = -\mathbf{R}'. \end{aligned} \tag{77}$$

In the above $[\mathbf{C}_P]$, $[\mathbf{C}_E]$, etc. are block coefficients and $\mathbf{R}'$ is a modified right-hand side vector. Equations of the form given by Eq. (77) provide for a fully implicit treatment of boundary conditions. Therefore, once the boundary equations coefficients have been specified, a block system of equations is completely defined for all inferior main grid points. It is important to reiterate that approximations made on the left-hand side operator will not affect the spatial or temporal accuracy of the scheme, so long as the solution converges in pseudo-time.

The block-banded system of equations represented by Eq. (77) can be solved using a variety of techniques. The present work employed the LU-factored scheme, which was originally proposed by Jameson and Turkel [15] as a means of constructing well-conditioned factorizations of implicit schemes for hyperbolic equations. It has

since been applied by many authors to the solution of the Euler and Navier–Stokes equations [16, 24, 39].

The LU scheme approximately factors the block-banded matrix operator $[\mathscr{M}]$ into the product of a lower diagonal operator $[\mathscr{L}]$ and an upper diagonal operator $[\mathscr{U}]$. Neglecting the second-order factorization error, the modified system can be written as

$$[\mathscr{L}][\mathscr{U}]\{\delta\mathbf{U}\} = -\{\mathbf{R}\}. \tag{78}$$

The solution of Eq. (78) is both simple and efficient. Defining

$$\{\delta\mathbf{U}^{**}\} \equiv [\mathscr{U}]\{\delta\mathbf{U}\}, \tag{79}$$

a forward sweep is performed to solve

$$[\mathscr{L}]\{\delta\mathbf{U}^{**}\} = \{\mathbf{R}\} \tag{80}$$

for $\{\delta\mathbf{U}^{**}\}$. This is followed by a backsweep to solve

$$[\mathscr{U}]\{\delta\mathbf{U}\} = \{\delta\mathbf{U}^{**}\} \tag{81}$$

for $\{\delta\mathbf{U}\}$. Since Eqs. (80) and (81) are triangular, the sweeps require only simple inversions of matrices.

4. RESULTS

In order to assess the accuracy, efficiency, and robustness of the surface capturing approach, extensive calculations were carried out for several two- and three-dimensional validation problems. Separate computer programs were written to compute the two- and three-dimensional problems. Although the general single-step, trapezoidal formulation presented in Section 3 was coded in both flow solvers, all calculations were performed using the Crank–Nicolson scheme ($\theta = \frac{1}{2}$), in order to provide second-order accuracy in time. In addition, exploratory calculations revealed that while the use of pseudo-time terms in the mass and momentum equations did promote the stability of the scheme for a given physical time step, it also tended to slow down the convergence of the subiteration process. Consequently, all calculations were performed without the pseudo-time terms in the mass and momentum equations. The faster convergence afforded by this arrangement appeared to compensate for the smaller physical time step required for stability.

In interpreting the solutions obtained using the surface capturing approach, it was important to unambiguously define the location of the free surface, based on the density distribution within the computational domain. Unlike surface fitting methods, the location of the free surface can only be approximated within the resolution provided by the grid. In the present work, the position of the free surface was defined as the surface of constant density for which $\rho(x, y, z) = \frac{1}{2}(\rho_1 + \rho_2) \equiv \rho_m$. All free surface plots presented in the sections below were created using 10 evenly spaced contours between $0.9\rho_m$ and $1.1\rho_m$.

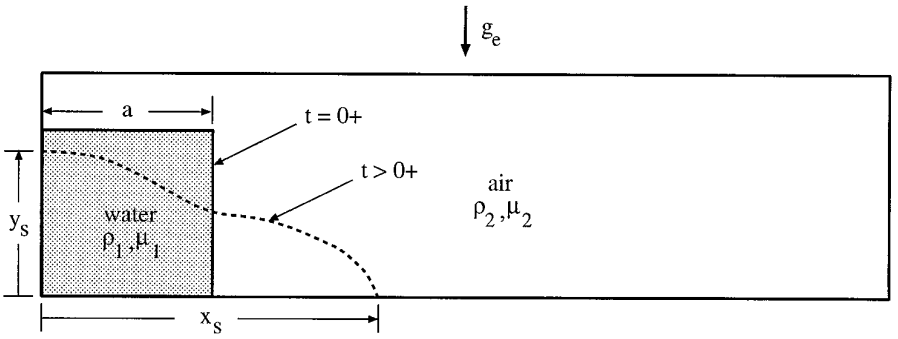

FIG. 2. Illustration of the two-dimensional broken dam problem.

4.1. *The Two-Dimensional Broken Dam Problem*

The sudden collapse of a rectangular column of fluid onto a horizontal surface is a classic problem in free surface hydrodynamics. Due to its use in modeling the sudden failure of a dam, it has become known as the broken dam problem. The relatively simple geometry and initial conditions associated with the broken dam problem has made it a popular validation case for various surface tracking and surface capturing schemes.

The specific geometry employed in the present work is illustrated in Fig. 2. A square water column a units wide is enclosed within an air-filled container $5a$ units long by $1.25a$ units high. The water is initially retained by a thin partition (the dam) on the right-hand side of the column. At time $t = 0+$, the partition is removed, thereby allowing the water to collapse under the influence of gravity. The specific configuration shown in Fig. 2 was chosen in order to approximate the collapsing water column experiments of Martin and Moyce [22]. Martin and Moyce used a high-speed camera to photograph the fluid motion at selected time intervals and thereby provide data for the free surface positions at the channel walls as functions of time.

Aside from the use of a two-dimensional model, the present geometry differs from the Martin and Moyce experiments in that the container in Fig. 2 is closed, whereas the channel used in the Martin and Moyce experiments was open to the atmosphere. However, since the density of water is much larger than the density of air, the use of a closed container should not have a significant effect on the motion of the water.

The initial conditions for the calculations were prescribed as follows. The density field was initialized with values appropriate for each fluid as shown in Fig. 2, the velocity components were set to zero everywhere, and the pressure distribution was arbitrarily defined to be hydrostatic relative to the top surface of the liquid. It should be noted that, since this problem involves an instantaneous change in the initial state of the two fluids (when the partition is removed), the true initial conditions at time $t = 0+$ will be different from those given above. The reason for this is that the hydrostatic pressure distributions along each side of the partition must equilibrate at time $t = 0+$, which, in turn, induces a nonzero velocity field.

TABLE II
Case Summary for the Two-Dimensional Broken Dam Problem

Case	Grid	$\Delta t/t_r$	Interpolant	Limiter (ρ)	*Re*
1	80×20	0.002	QUICK	Comp. minmod	42792
2	120×30	0.00133	QUICK	Comp. minmod	42792
3	160×40	0.001	QUICK	Comp. minmod	42792
4	80×20	0.001	QUICK	Comp. minmod	42792
5	80×20	0.002	QUICK	Comp. minmod	121033
6	80×20	0.002	1^{st} order upwind	N/A	42792
7	80×20	0.002	2^{nd} order upwind	Comp. minmod	42792
8	80×20	0.002	QUICK	Minmod	42792
9	80×20	0.002	QUICK	Van Leer	42792
10	80×20	0.002	QUICK	Superbee	42792

This condition appears to develop naturally at the first time step of the numerical algorithm, and the calculations to date have not been adversely affected by the use of the simpler initial conditions.

A total of 10 cases were computed for the present study. The key parameters associated with these cases are summarized in Table II. Reference quantities for nondimensionalization were selected as follows: $L_r = a$; $V_r = \sqrt{g_e a}$; $t_r = \sqrt{a/g_e}$; $\rho_r = \rho_1$; and $\mu_r = \mu_1$. The pseudo-compessibility parameter, β, was set to 5×10^4 N/m^2.

For the case of a square column of water, Martin and Moyce obtained data at two different length scales: $a = 0.05715$ m and $a = 0.1143$ m. With the reference quantities defined above, the corresponding Reynolds numbers ($\mathrm{Re} = \rho_r V_r L_r/\mu_r$) were 42792 and 121033. Both Reynolds numbers were examined in this study.

After extensive exploratory calculations, a baseline case (Case 1 in Table II) was established using a uniform grid of 80×20 control volumes and a length scale of $a = 0.05715$ m. These baseline results were then used as a reference for other cases. All calculations were allowed to proceed until the surge front reached the forward wall of the container.

To establish the grid independence of the solutions relative to the baseline case, calculations were also made using uniform grids of 120×30 and 160×40 control volumes (Cases 2 and 3). The time step was reduced in both cases to maintain a constant reference CFL number ($V_r\, \Delta t/\Delta x$). A separate case was also computed to demonstrate the effect of reducing the time step on the baseline grid (Case 4).

The computed surge front and column height positions (nondimensionalized with respect to a) for Cases 1–4 are plotted with respect to the nondimensional time in Figs. 3 and 4. The data of Martin and Moyce are also plotted for comparison. From these plots, it can be seen that the baseline results are essentially grid independent. In addition, the numerical solutions compare well with experimental data, considering the uncertainties inherent in the experimental data and the approximations employed in the numerical model. However, the computed surge front position does appear to diverge somewhat from the experimental data toward the end of the transient.

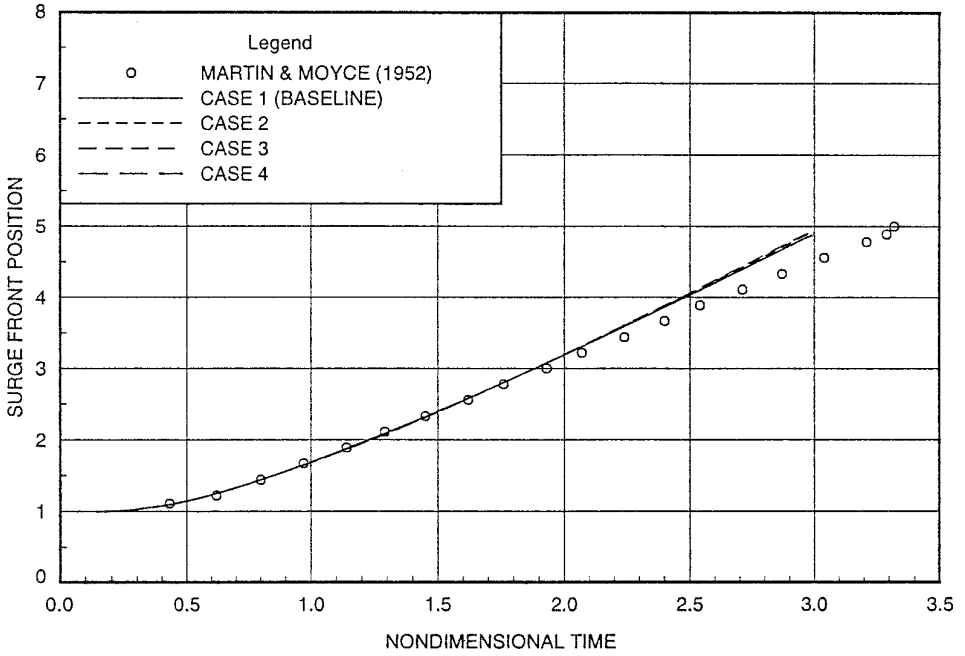

FIG. 3. Surge front position versus time for $a = 0.05715$ m.

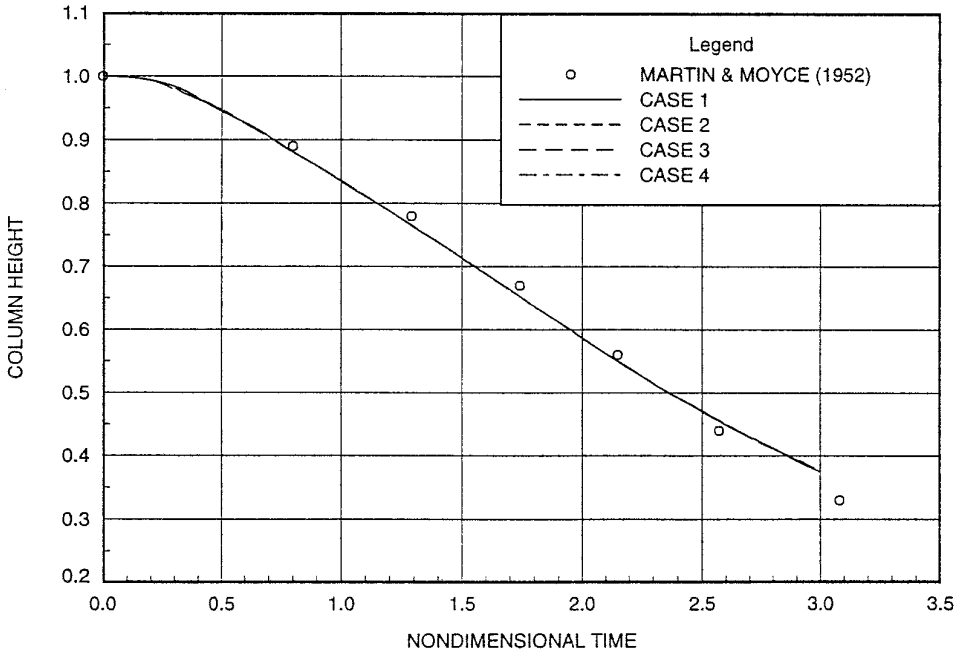

FIG. 4. Column height versus time for $a = 0.05715$ m.

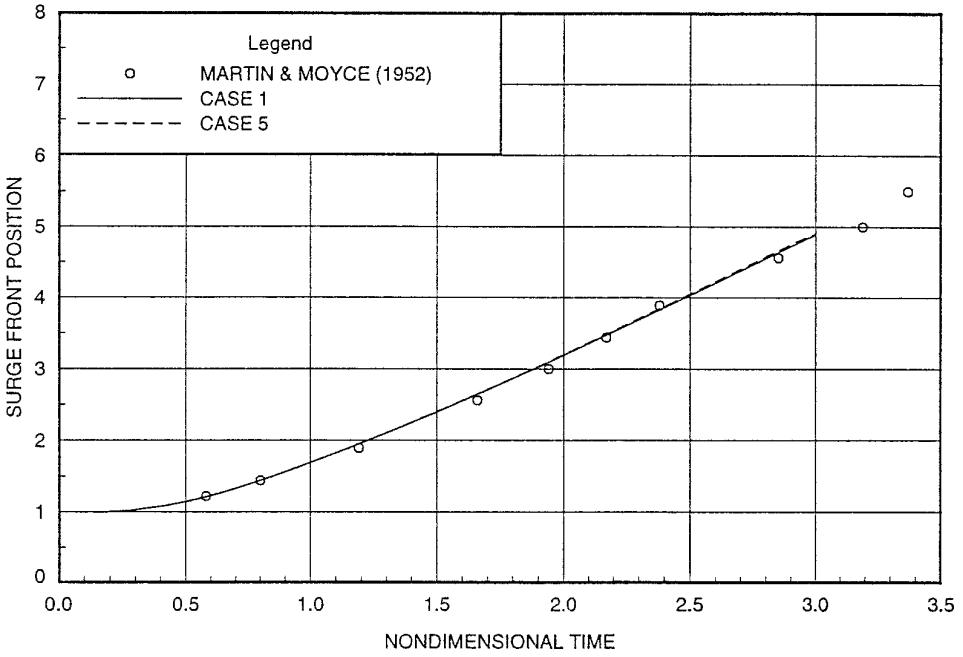

FIG. 5. Surge front position versus time for $a = 0.1143$ m.

To examine the effect of Reynolds number, a separate high Reynolds number calculation was performed on the baseline grid using $a = 0.1143$ m (Case 5). A comparison of these results with both the baseline case and the $a = 0.1143$ m data of Martin and Moyce is shown in Figs. 5 and 6 (note that the Martin and Moyce data in Fig. 6 are for $a = 0.05715$ m, since measurements for this Reynolds number were not reported). The close agreement of the two numerical solutions suggests that increasing the Reynolds number relative to the baseline case does not significantly affect the free surface motion. Moreover, the high Reynolds number results appear to agree more closely with the data of Martin and Moyce. It is not clear whether or not this indicates that the primary source of the discrepancy observed at the lower Reynolds number is due to uncertainties in the experimental data, or perhaps, to some other effect not accounted for by the two-dimensional model.

The free surface and velocity fields for the 160×40 control volume grid (Case 3) are plotted at selected times in Figs. 7 and 8. Initially, the large difference between the hydrostatic pressure distribution in the water relative to the adjacent air creates a large horizontal pressure gradient at the bottom of the dam. This, in turn, accelerates the fluid along the bottom of the container. Eventually, an elongated fluid layer develops as the surge front sweeps toward the front of the container. An interesting feature of this flow field is the vortex which forms in the vicinity of the free surface.

The effect of various upwind-biased interpolation schemes and the density limiter functions on the numerical solution were examined in Cases 6–10. Comparisons of solution quality were made using the sharpness of the density profile at the water–air interface as a figure of merit. Experience with the surface capturing method has

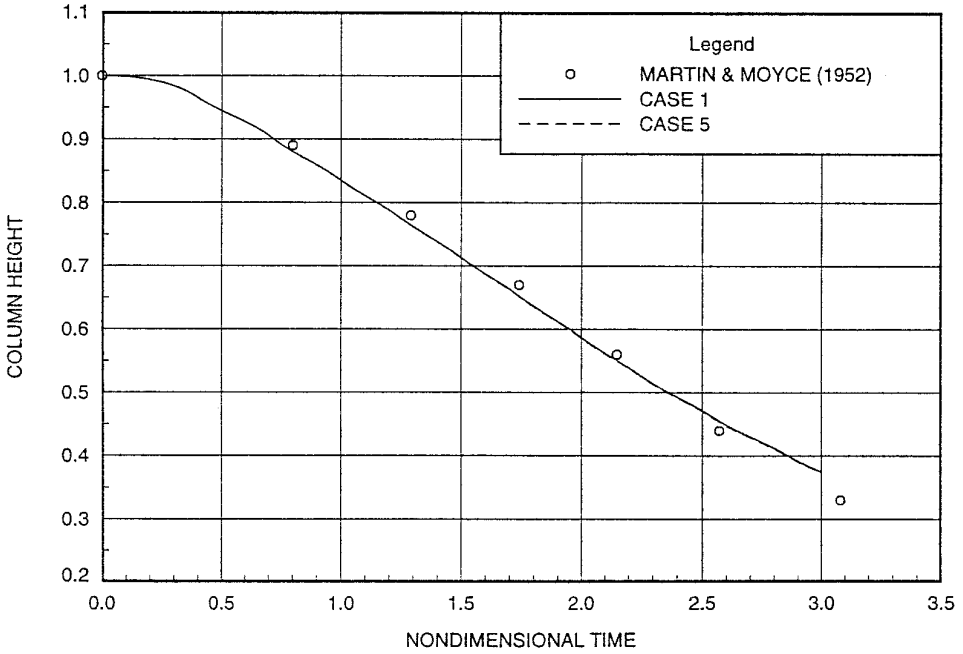

FIG. 6. Column height versus time for $a = 0.1143$ m.

shown that it is important to prevent excessive diffusion of the density interface in order to maintain the accuracy of the solution for long time periods.

Since the velocity field is continuous for viscous flows, no limiters were applied to the interpolation of the velocity components. While pressure field itself is also continuous, there will be a jump in the pressure gradient across the free surface. Therefore, a simple minmod limiter was used in the interpolation of the pressure.

In Fig. 9, the density profiles along the bottom wall of the container at time $t/t_r = 1.5$ are plotted for solutions using first order upwind, second-order upwind, and QUICK interpolants for all variables. Both the second-order upwind and QUICK cases used a compressive minmod limiter for density (no limiting is necessary for the first-order upwind interpolant). As expected, first-order upwind interpolation produced a highly smeared density profile, whereas the higher order interpolants yielded substantially sharper profiles. Overall, the QUICK profile was the best of the three.

The impact of the limiter function on the density profile is shown in Fig. 10. Again, the density profiles along the bottom wall of the container at time $t/t_r = 1.5$ are plotted. It can be seen that the minmod limiter is the most diffusive and the superbee limiter the least. While these results would seem to favor the use of the superbee limiter, experience has shown that calculations using the superbee limiter are not as robust as those for the other limiters. This behavior is consistent with results reported in the literature for explicit and implicit TVD MUSCL schemes [40]. Fortunately, the compressive minmod limiter produced profiles which were comparable to the superbee limiter without the attendant robustness problems.

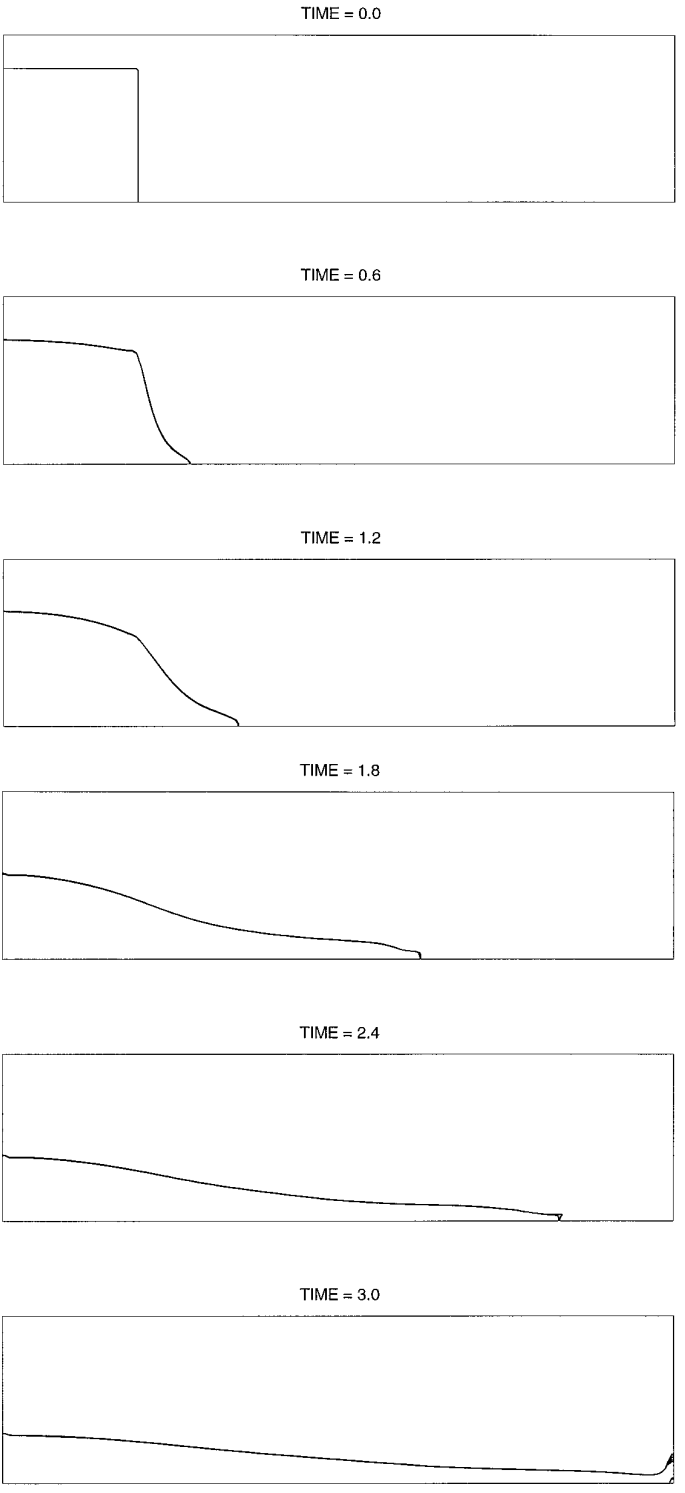

FIG. 7. Free surface motion for two-dimensional broken dam problem.

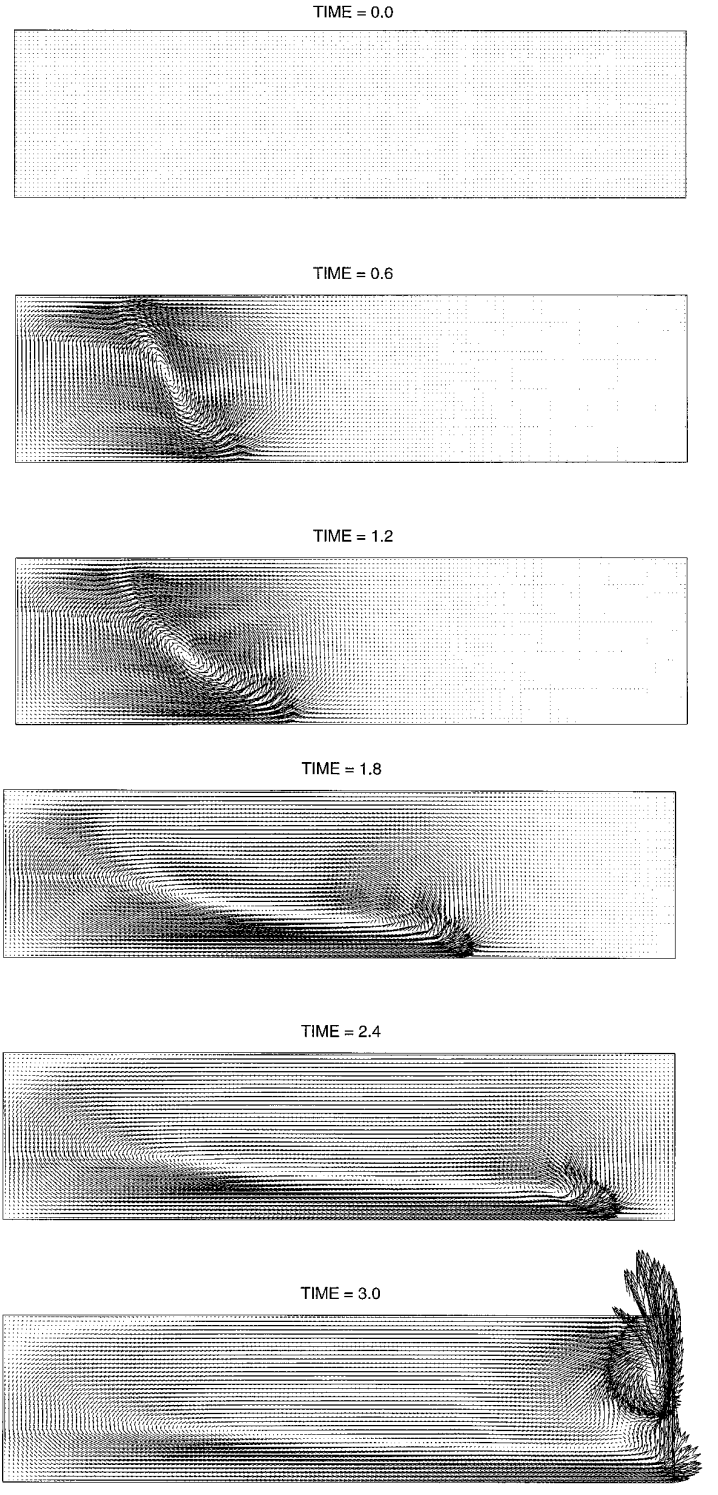

FIG. 8. Velocity field for two-dimensional broken dam problem.

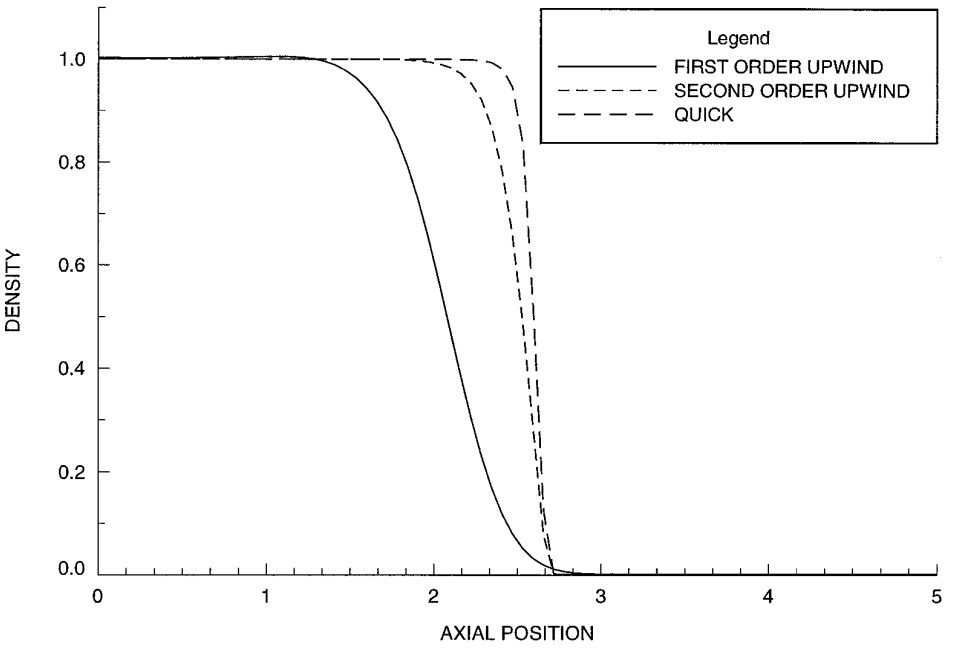

FIG. 9. Comparison of density profiles for first- and third-order interpolants.

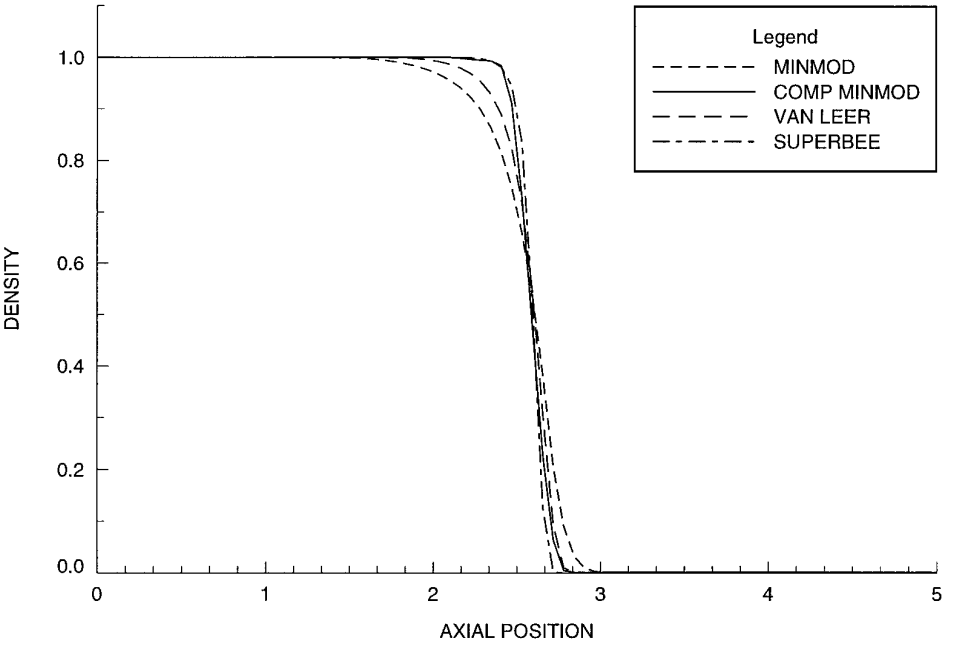

FIG. 10. Comparison of density profiles for various limiters.

Based on the foregoing results, all subsequent two- and three-dimensional calculations were performed using the QUICK interpolants for all variables, and the compressive minmod limiter for density. While this combination has proven adequate for the calculations performed to date, additional study would be required to determine if other combinations of interpolants and limiters (including some not listed here) would be superior to these.

For all of the broken dam cases, the conservation of total mass was monitored by summing the fluid mass ($\rho\Omega$) within each control volume over the entire computational domain. In every case, the change in total mass over the duration of the transient was less than 0.01%. Similar levels of mass conservation were maintained in all subsequent two- and three-dimensional calculations.

Finally, an important link between the nondimensional pseudo-compressibility parameter β and the computed density field was revealed in the broken dam calculations. Specifically, it was found that setting β too low (on the order of 10^0–10^1) produced large, unphysical oscillations in the density near the free surface. An analysis of a simple one-dimensional analog of the two-fluid equations confirmed this connection. Numerical experiments showed that this problem could be effectively suppressed by prescribing a larger value of β (generally on the order of 10^3–10^4). However, making β too large tended to promote divergence of the pseudo-time marching process. It was concluded that an ''optimal'' value of β must exist which provides sufficient suppression of density oscillations without significantly affecting the convergence properties of the numerical algorithm. To date, an appropriate value of β for a particular problem has been determined through trial and error.

4.2. *The Two-Dimensional Rayleigh–Taylor Instability*

When a horizontal layer of heavy fluid overlies a layer of light fluid in the presence of a vertical gravitational field, the interface between the two fluids is unstable. If the interface is perturbed, buoyancy forces will cause the amplitude of the perturbation to grow with time. This phenomenon is known as the Rayleigh–Taylor instability. The original problem, as formulated by Rayleigh [27] and Taylor [34], was concerned with a linear perturbation analysis for the case of two inviscid, incompressible fluid layers. Other investigators extended the linear analysis to include the effects of viscosity and surface tension [6]. More recently, CFD methods have been used to obtain numerical solutions to the full, nonlinear problem [9, 13, 41, 35].

The present work considers the Rayleigh–Taylor instability for two viscous, incompressible fluid layers with a prescribed density ratio (ρ_1/ρ_2) of two and a uniform kinematic viscosity ($\nu_1 = \nu_2$). As illustrated in Fig. 11, the fluids are confined within a periodic domain of width $2L$ and height H which is bounded above and below by impermeable walls. The flow field is assumed to be symmetric about $x = 0$.

A single wavelength perturbation is introduced at the fluid interface using the following nondimensional initial velocity field, which was adapted from the work of Daly [9]:

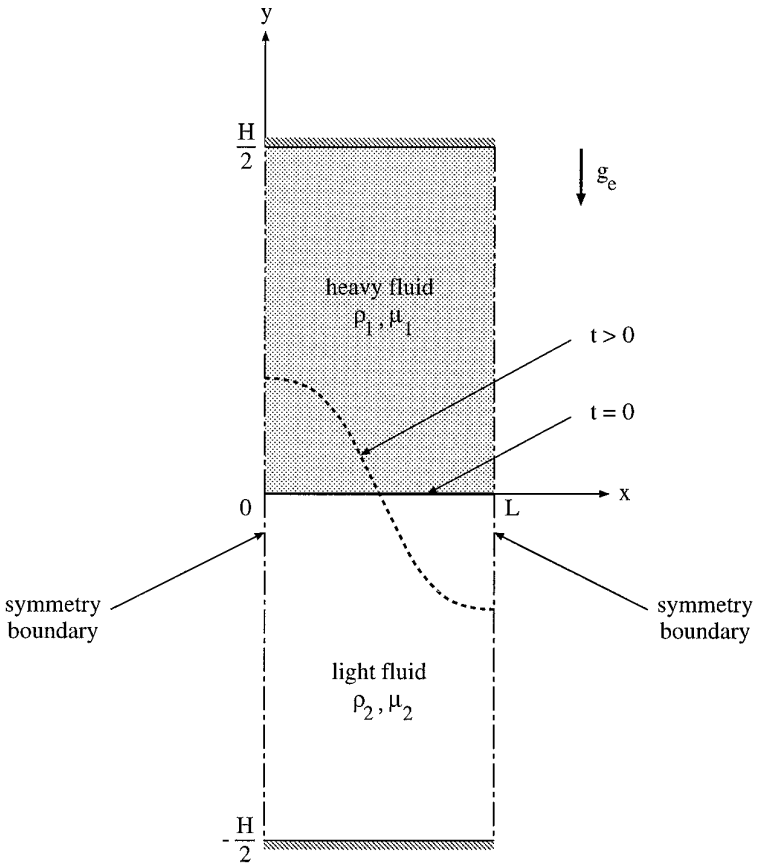

FIG. 11. Illustration of the Rayleigh–Taylor instability problem.

$$\frac{u}{V_r} = \begin{cases} \alpha \sin\left(\dfrac{\pi x}{L}\right) \exp\left(-\dfrac{\pi |y|}{L}\right), & \dfrac{y}{L} > 0, \\ -\alpha \sin\left(\dfrac{\pi x}{L}\right) \exp\left(-\dfrac{\pi |y|}{L}\right), & \dfrac{y}{L} < 0, \end{cases} \tag{82}$$

$$\frac{v}{V_r} = \alpha \cos\left(\frac{\pi x}{L}\right) \exp\left(-\frac{\pi |y|}{L}\right) \tag{83}$$

$$\alpha = \frac{\pi A\, \Delta y}{2 V_r L}. \tag{84}$$

Here, A is a perturbation amplitude and Δy is a representative mesh increment in the vertical direction. This velocity field corresponds to a sinusoidal perturbation of wavelength $2L$. To conplete the specification of the initial conditions, the density field was prescribed as shown in Fig. 11, while the initial pressure was set to a hydrostatic distribution.

TABLE III
Case Summary for Large Perturbation Amplitude Rayleigh–Taylor Instability Calculations

Case	Grid	μ_1 ($N - s/m^2$)	μ_2 ($N - s/m^2$)	$\Delta t/t_r$	Re
1	30×90	2×10^{-4}	1×10^{-4}	0.001	28.3
2	30×90	2×10^{-5}	1×10^{-5}	0.001	283
3	40×120	2×10^{-4}	1×10^{-4}	0.001	28.3
4	40×120	2×10^{-5}	1×10^{-5}	0.001	283

Four cases were run initially for a perturbation amplitude $A = 1$ to obtain solutions for Reynolds numbers of 28.3 and 283 on uniform grids of 30×90 and 40×120 control volumes. The key parameters for these four cases are presented in Table III. All calculations were carried out for 4800 time steps, with $\Delta t/t_r = 0.001$, and the pseudo-compressibility parameter set to 1×10^3 N/m^2. Reference quantities for nondimensionalization were selected as follows: $L_r = L$, $V_r = \sqrt{g_e L}$, $t_r = \sqrt{L/g_e}$, $\rho_r = \rho_1$, and $\mu_r = \mu_1$.

The effect of Reynolds number on the evolution of the free surface is illustrated in Figs. 12–13 (results for the 40×120 control volume grid are shown). In both cases, the initial perturbation causes the light fluid to rise along the left boundary and the heavy fluid to sink along the right boundary. The displacement of the interface is seen to be nearly symmetric during the early growth phase of the instability. As the amplitude of the instability increases, the characteristic mushroom shape emerges in the vicinity of the central vortex. The rollup of the interface is much more pronounced for the higher Reynolds number case due to the smaller influence of viscous effects, which would tend to smooth out sharp velocity gradients. Eventually, the walls begin to influence the solution during the latter stages of the transient, especially in the high Reynolds number case. To permit the interface to develop unimpeded for longer times, a larger computational domain would be required.

According to linear theory, viscosity has a significant effect on the growth rate of a single wavelength perturbation. Specifically, it is found that as the perturbation wavelength decreases, the growth rate increases without bound in the absence of viscosity, while the growth rate for the viscous case approaches zero. At large perturbation wavelengths, however, the predicted growth rates for both the inviscid and viscous cases approach zero. It follows that a maximum growth rate must exist for the viscous case at some intermediate perturbation wavelength.

For the specific case of equal kinematic viscosities ($\nu_1 = \nu_2 = \nu$), Chandrasekhar [6] derived a relation between the linear growth rate and the perturbation wavelength. This variation can be expressed in terms of a nondimensional growth rate $n^* = n\nu^{1/3}/g_e^{2/3}$ and a modified Reynolds number $\mathrm{Re_m} = \lambda_p^{3/2} g_e^{1/2}/\nu$, where n is the dimensional growth rate (with units of $1/s$) and $\lambda_p = 2L$ is the perturbation wavelength. From this result, Chandrasekhar was able to determine the maximum growth rate and its corresponding wavelength for a given density ratio, kinematic viscosity, and gravitational acceleration.

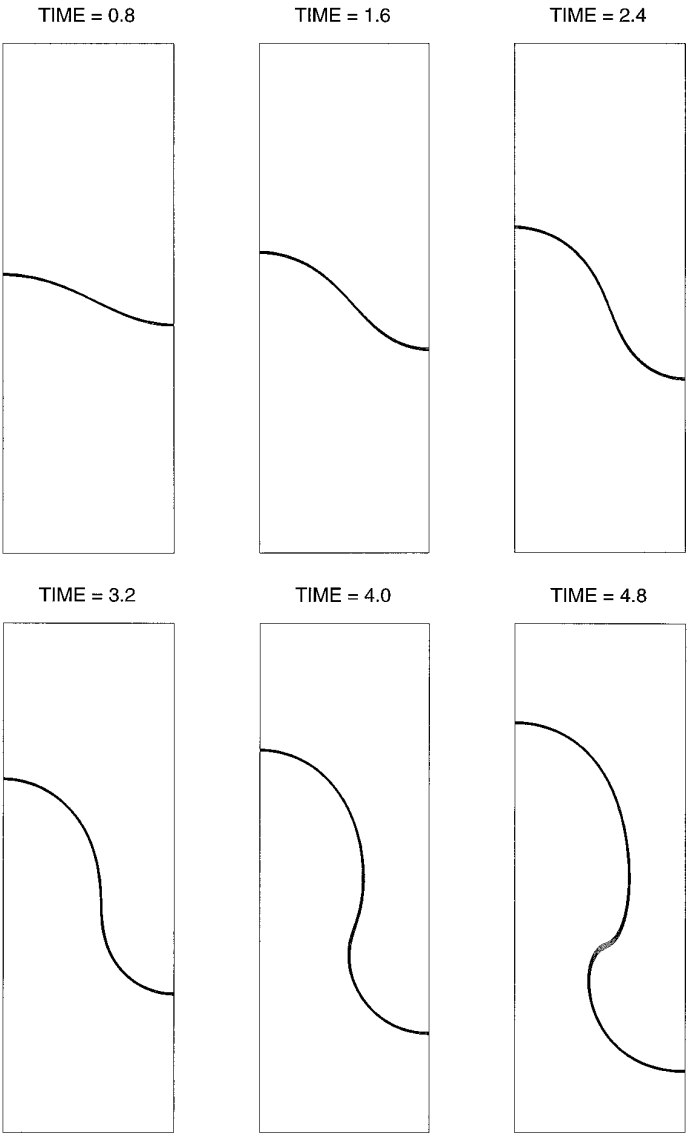

FIG. 12. Free surface motion for the Rayleigh–Taylor instability; Re = 28.3.

To determine if the present surface capturing method could reproduce the growth rates predicted by linear analysis, a series of calculations was performed for a density ratio of two using four values of kinematic viscosity to provide a range of modified Reynolds numbers. The perturbation amplitude for these calculations was reduced by an order of magnitude ($A = 0.1$) to help maintain the linear behavior of the solution over the duration of the transient.

The growth rate for each case was calculated from the numerical results using a procedure adapted from [9]. This procedure is based on the fact that the amplitude of the interface displacement grows exponentially in time such that, after initial transients have died away, a single positive growth rate emerges. When this occurs,

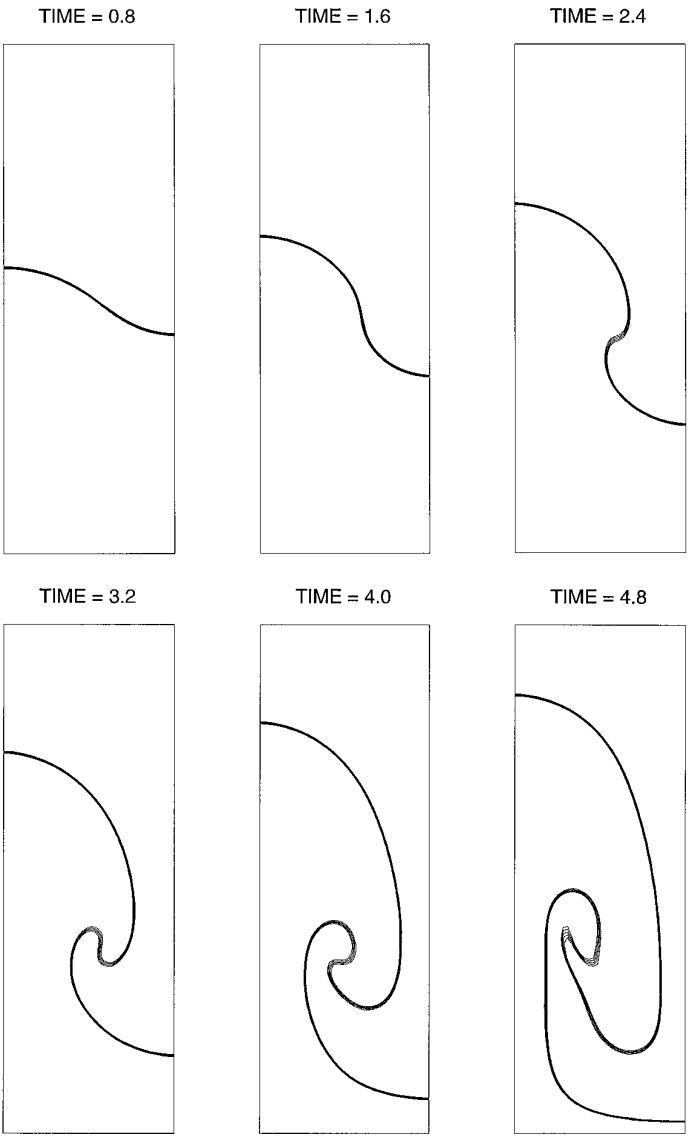

FIG. 13. Free surface motion for the Rayleigh–Taylor instability; Re = 283.

the natural logarithm of the interface displacement should vary linearly with time, the slope of this line being the growth rate.

The calculations for all four cases were performed on a uniform 30×90 control volume grid. The key parameters are summarized in Table IV.

A comparison of the computer growth rates with the growth rate variation predicted by the linear analysis of Chandrasekhar is given in Fig. 14. The numerical results show good agreement with the theoretical curve and appear to reproduce the expected decrease in growth rate at small and large modified Reynolds numbers. The minor discrepancies exhibited by the numerical results can be attributed to the slight departure of the numerical solution from linear behavior.

TABLE IV
Case Summary for Small Perturbation Amplitude Rayleigh–Taylor Instability Calculations

Case	Grid	μ_1 $(N - s/m^2)$	μ_2 $(N - s/m^2)$	Re_m
1	30×90	8×10^{-4}	4×10^{-4}	20
2	30×90	2×10^{-4}	1×10^{-4}	80
3	30×90	8×10^{-5}	4×10^{-5}	200
4	30×90	2×10^{-5}	1×10^{-5}	800

4.3. *The Three-Dimensional Broken Dam Problem*

As a first test case for the three-dimensional surface capturing algorithm, calculations were carried out for a three-dimensional version of the broken dam problem. As illustrated in Fig. 15, the geometry is essentially the same as in the two-dimensional case, except that the container is now assumed to have a finite width a in the z coordinate direction. Due to the symmetry of the flow field, only half of the channel was used as the computational domain, with a symmetry plane established at $z = 0.5a$.

The calculations were made using a uniform grid of $80 \times 20 \times 10$ control volumes and a length scale of $a = 0.05715$ m. The initial conditions and reference quantities for nondimensionalization were identical to those employed in the two-dimensional case.

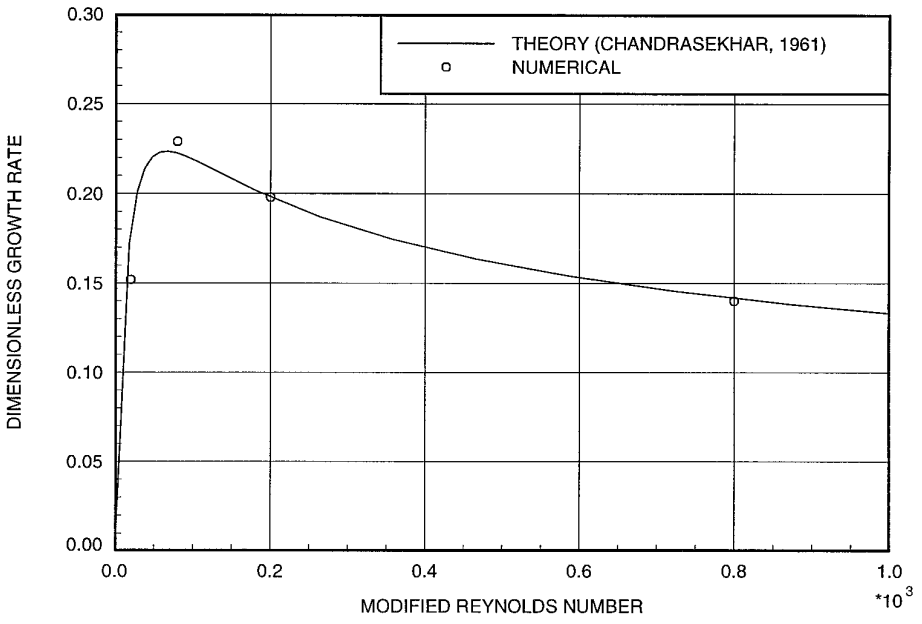

FIG. 14. Nondimensional perturbation growth rate versus modified Reynolds number—comparison of numerical results with linear theory.

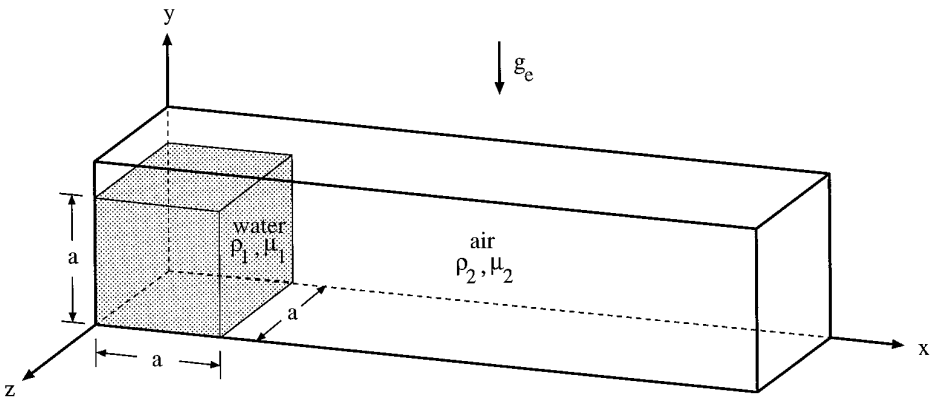

FIG. 15. Illustration of the three-dimensional broken dam problem.

Plots of the surge front and column height positions at the symmetry plane of the channel are presented in Figs. 16 and 17. Also plotted in these figures are the experimental data of Martin and Moyce and the corresponding results for the two-dimensional broken dam problem. From these plots, it can be seen that there is very little difference between the two- and three-dimensional solutions. This is probably due to the high Reynolds number for this particular case, which reduced the influence of the side walls on the flow field at the symmetry plane.

The motion of the free surface within the half channel is depicted in Fig. 18. Here, density contours lines were plotted on each boundary surface to provide an

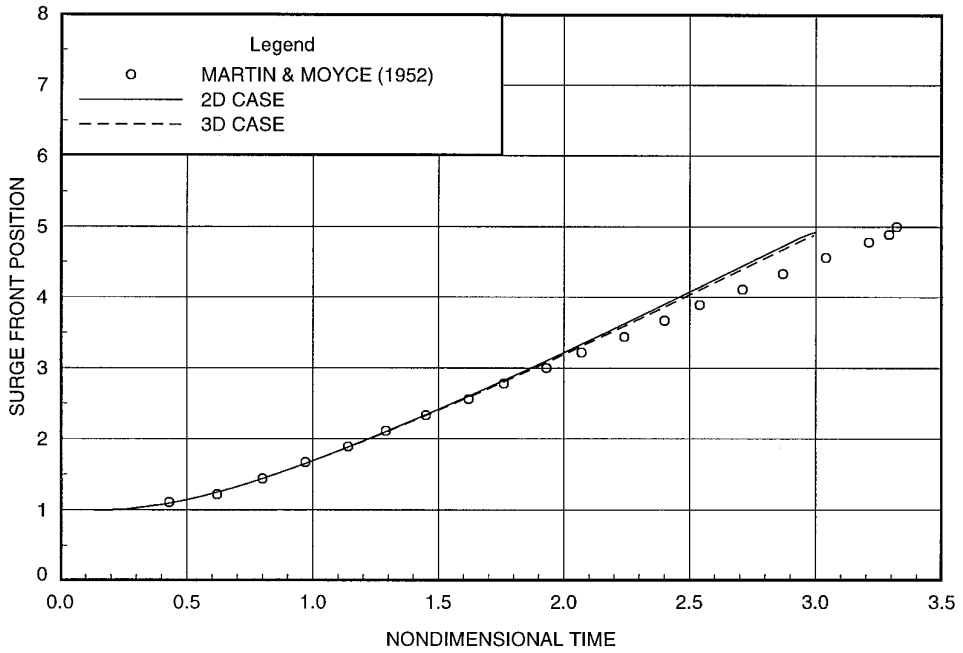

FIG. 16. Surge front position versus time for $a = 0.05715$ m.

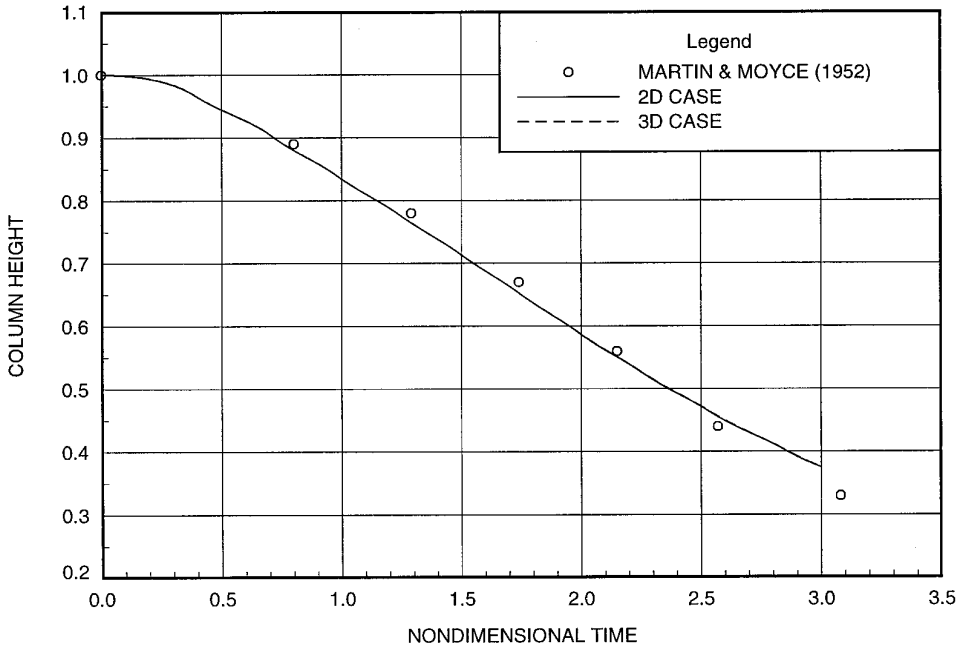

FIG. 17. Column height versus time for $a = 0.05715$ m.

illustration of the three-dimensional free surface motion. It is seen that the free surface does not deform appreciably across the channel and that the shape of the interface is similar to those shown previously for the two-dimensional case. The velocity fields at the symmetry plane and at several cross channel stations are shown in Figs. 19 and 20. As in the two-dimensional case, a large vortex is observed in the vicinity of the density interface. Also, some three-dimensionality of the flow is observed in the cross channel velocity plots.

5. CONCLUSIONS

The preceding sections have described the development of a new surface capturing method for computing viscous free surface flows in partially filled containers. The algorithm employed the artificial compressibility method and a dual time stepping strategy to develop a conservative, implicit, finite volume formulation of the equations of motion for a viscous, incompressible, variable density fluid. The use of a consistent formulation in both the liquid and gas regions permitted the free surface to be automatically captured as a discontinuity in the density, and thereby eliminated the need for special free surface tracking procedures.

An extensive set of validation calculations were carried out for the two-dimensional broken dam problem in order to examine the effects of grid refinement (in

FIG. 18. Free surface motion for the three-dimensional broken dam problem.

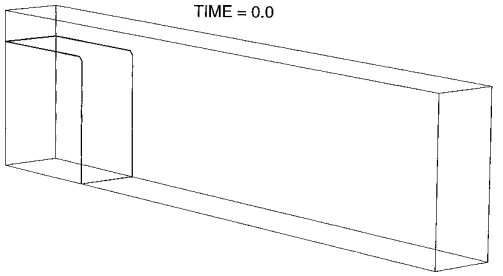
TIME = 0.0

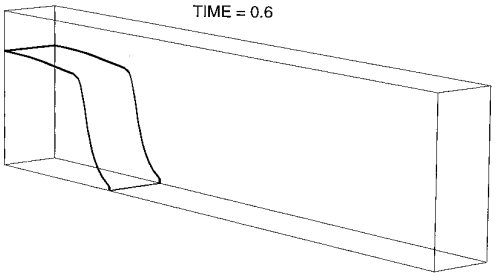
TIME = 0.6

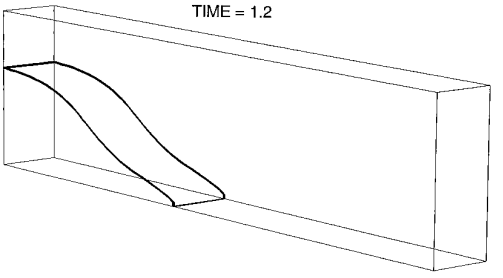
TIME = 1.2

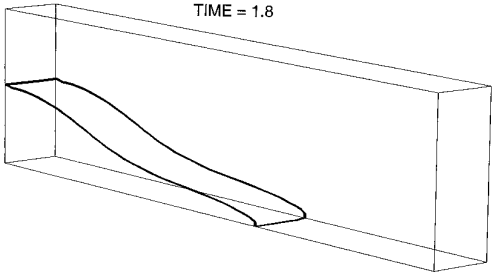
TIME = 1.8

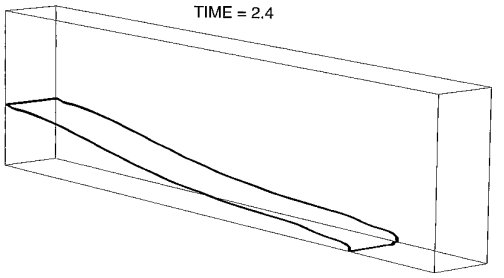
TIME = 2.4

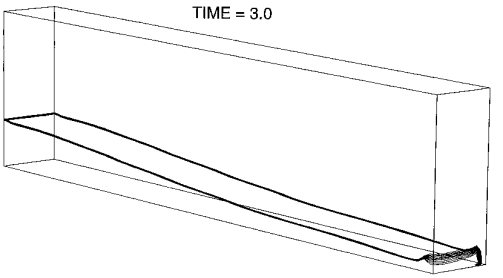
TIME = 3.0

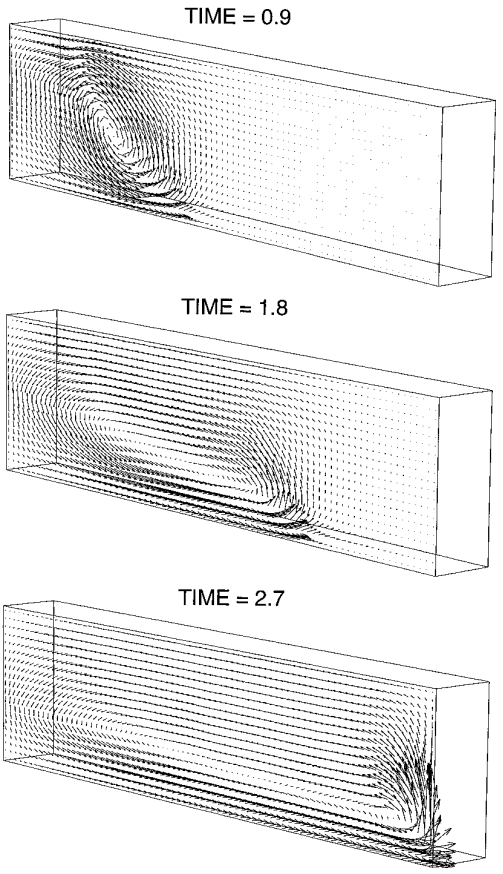

FIG. 19. Symmetry plane velocity fields for the three-dimensional broken dam problem at selected times.

both space and time), Reynolds number, upwind-biased interpolants, and limiter functions. The computed solutions were found to be relatively insensitive to grid refinement and Reynolds number. A comparison of computed surge front column height positions as functions of time showed reasonably good agreement with the experimental data of Martin and Moyce. In addition, the free surface profiles (plotted as density contours about the mean density value) compared favorably with photographs from the Martin and Moyce experiments. The choice of interpolant and limiter functions used in the inviscid flux construction was found to have a significant impact on the level of numerical diffusion at the free surface. Specifically, it was shown that the best solutions (in terms of computed density profiles) were obtained by using the QUICK interpolant for all variables, the compressive minmod limiter for the density, the minmod limiter for pressure, and no limiting on the velocities. This combination of interpolants and limiters was adopted in all subsequent calculations. Total mass conservation checks showed less than 0.01% change over the transient, a result which was replicated in all calculations performed in this study. Finally, numerical experiments with the broken dam problem revealed that the

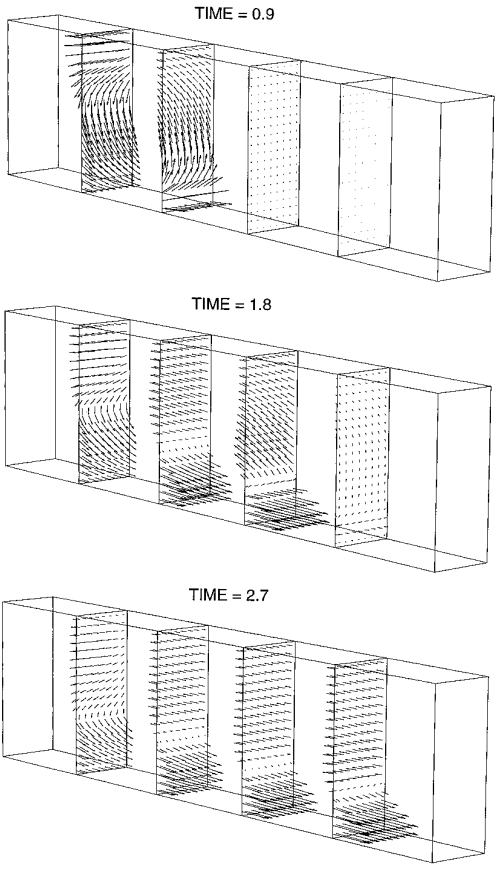

FIG. 20. Cross channel velocity fields for the three-dimensional broken dam problem at selected times.

pseudo-compressibility parameter must be made suitably large in order to suppress the formation of unphysical oscillations in the density field near the free surface. Solutions computed for the two-dimensional Rayleigh–Taylor problem demonstrated the present scheme's ability to capture complex interfacial motions, particularly for high Reynolds number cases. A series of calculations for linear (early time) growth rate of the sinusoidal perturbation showed good agreement between the analytical results of Chandrasekhar and numerical predictions. Finally, calculations for a three-dimensional version of the broken dam problem were performed in order to validate the three-dimensional surface capturing formulation. The computed surge front and column height positions at the symmetry plane were found to agree with both the data of Martin and Moyce and a previously computed two-dimensional solution.

Although the present method has been tested using simple geometries, the formulation is of sufficient generality to permit free surface flows in more complex geometries to be computed. It is entirely possible, for example, to employ the present method within an unstructured grid, finite-volume solution scheme. Such a scheme

could use solution-adaptive gridding to points in the vicinity of the free surface and thereby reduce the smearing of the density gradient as the free surface evolves. In addition, the present approach should be able to incorporate surface tension models, such as the scheme proposed by Brackbill *et al.* [5]. Such modeling would clearly be required for computing capillary flows, bubble and droplet dynamics, and flows in microgravity environments.

APPENDIX

A. *The Inviscid Flux Jacobians*

The solution vector $\mathbf{U}$ and the inviscid flux vector $\mathbf{F}_{\text{inv}} \equiv \mathbf{F}_{\text{inv}} \cdot \mathbf{S}$ for the three-dimensional equations are given by

$$\mathbf{U} = \begin{bmatrix} \rho \\ \rho u \\ \rho v \\ \rho w \\ P \end{bmatrix} \tag{85}$$

$$\mathbf{F}_{\text{inv}} = \begin{bmatrix} \rho q \\ \rho q u + \beta P S_x \\ \rho q v + \beta P S_y \\ \rho q w + \beta P S_z \\ q \end{bmatrix}, \tag{86}$$

where $P = p/\beta$ and

$$q = \mathbf{V} \cdot \mathbf{S} = uS_x + vS_y + wS_z \tag{87}$$

$$\mathbf{S} = S_x \hat{\imath} + S_y \hat{\jmath} + S_z \hat{k}. \tag{88}$$

The inviscid Jacobian matrix $[\mathbf{A}_{\text{inv}}] \equiv \partial \mathbf{F}_{\text{inv}}/\partial \mathbf{U}$ is given by

$$[\mathbf{A}_{\text{inv}}] = \begin{bmatrix} 0 & S_x & S_y & S_z & 0 \\ -qu & q + uS_x & uS_y & uS_z & \beta S_x \\ -qv & vS_x & q + vS_y & vS_z & \beta S_y \\ -qw & wS_x & wS_y & q + wS_z & \beta S_z \\ -q/\rho & S_x/\rho & S_y/\rho & S_z/\rho & 0 \end{bmatrix}. \tag{89}$$

B. *The Eigensystem of the Inviscid Flux Jacobians*

The five eigenvalues of the inviscid flux Jacobian matrix $[\mathbf{A}_{\text{inv}}]$ are derived from the determinant

$$|[\mathbf{A}_{\text{inv}}] - \lambda_l[\mathbf{I}]| = 0, \tag{90}$$

where λ_l denotes the l^{th} eigenvalue. The m right eigenvectors are then obtained by solving the system for each eigenvalue,

$$([\mathbf{A}_{\text{inv}}] - \lambda_l[\mathbf{I}])\,\mathbf{V}_l = 0, \tag{91}$$

where $\mathbf{V}_l$ is the l^{th} right eigenvector of $[\mathbf{A}_{\text{inv}}]$. The matrix whose columns are the right eigenvectors taken in order is denoted $[\mathbf{T}]$ and its inverse $[\mathbf{T}]^{-1}$. Since $[\mathbf{A}_{\text{inv}}]$ has real eigenvalues and a linearly independent set of right eigenvectors (to be defined below), then the similarity relation

$$[\mathbf{A}_{\text{inv}}] = [\mathbf{T}][\Lambda][\mathbf{T}]^{-1} \tag{92}$$

holds. Here, $[\Lambda]$ is the diagonal eigenvalue matrix,

$$[\Lambda] = \text{diag}(\lambda_1, \lambda_2, \ldots, \lambda_m). \tag{93}$$

For the three-dimensional inviscid flux Jacobian presented in Appendix A, the eigenvalues are

$$\lambda_1 = \lambda_2 = \lambda_3 = q \tag{94}$$

$$\lambda_{4,5} = \tfrac{1}{2}(q \pm c), \tag{95}$$

where

$$c \equiv \sqrt{q^2 + 4\beta'(S_x^2 + S_y^2 + S_z^2)} \tag{96}$$

$$\beta' \equiv \frac{\beta}{\rho} \tag{97}$$

and $\mathbf{S} = S_x\hat{\imath} + S_y\hat{\jmath} + S_z\hat{k}$ is either $\mathbf{S}^\xi$, $\mathbf{S}^\eta$, or $\mathbf{S}^\zeta$.

The dependence of the right eigenvectors on the geometry produces minor differences in the elements of $[\mathbf{T}]$ and $[\mathbf{T}]^{-1}$ for each computational coordinate direction (ξ, η, ζ). Accordingly, the specific forms of these matrices for each direction are presented below. For convenience, the following notation is used:

$$S = \sqrt{S_x^2 + S_y^2 + S_z^2} \tag{98}$$

$$\mathbf{g}^\xi = \frac{\partial \mathbf{r}}{\partial \xi} \times \mathbf{S} \tag{99}$$

$$\mathbf{g}^\eta = \frac{\partial \mathbf{r}}{\partial \eta} \times \mathbf{S} \tag{100}$$

$$\mathbf{g}^\zeta = \frac{\partial \mathbf{r}}{\partial \zeta} \times \mathbf{S}. \tag{101}$$

In the above, $\mathbf{r} = x\hat{\imath} + y\hat{\jmath} + z\hat{k}$. Note that the metric derivatives required in these matrices ($\partial x/\partial\xi$, $\partial x/\partial\eta$, etc.) are approximated using finite differences:

- ξ direction,

$$[\mathbf{T}^{\xi}] = \begin{bmatrix} 1 & 0 & 0 & \lambda_4 & \lambda_5 \\ u & \partial x/\partial \eta & \partial x/\partial \zeta & u\lambda_4 + \beta' S_x & u\lambda_5 + \beta' S_x \\ v & \partial y/\partial \eta & \partial y/\partial \zeta & v\lambda_4 + \beta' S_y & v\lambda_5 + \beta' S_y \\ w & \partial z/\partial \eta & \partial z/\partial \zeta & w\lambda_4 + \beta' S_z & w\lambda_5 + \beta' S_z \\ 0 & 0 & 0 & -\lambda_5/\rho & -\lambda_4/\rho \end{bmatrix} \tag{102}$$

$$[\mathbf{T}^{\xi}]^{-1} = \begin{bmatrix} 1 + q^2/\beta' S^2 & -qS_x/\beta' S^2 & -qS_y/\beta' S^2 & -qS_z/\beta' S^2 & -\rho \\ -\mathbf{g}^{\zeta} \cdot \mathbf{V}/S^2 & \mathbf{g}^{\zeta} \cdot \hat{\imath}/S^2 & \mathbf{g}^{\zeta} \cdot \hat{\jmath}/S^2 & \mathbf{g}^{\zeta} \cdot \hat{k}/S^2 & 0 \\ \mathbf{g}^{\eta} \cdot \mathbf{V}/S^2 & -\mathbf{g}^{\eta} \cdot \hat{\imath}/S^2 & -\mathbf{g}^{\eta} \cdot \hat{\jmath}/S^2 & -\mathbf{g}^{\eta} \cdot \hat{k}/S^2 & 0 \\ -q\lambda_4/\beta' S^2 c & \lambda_4 S_x/\beta' S^2 c & \lambda_4 S_y/\beta' S^2 c & \lambda_4 S_z/\beta' S^2 c & \rho/c \\ q\lambda_5/\beta' S^2 c & -\lambda_5 S_x/\beta' S^2 c & -\lambda_5 S_y/\beta' S^2 c & -\lambda_5 S_z/\beta' S^2 c & -\rho/c \end{bmatrix}, \tag{103}$$

where $\mathbf{S}$, q, λ_4, λ_5, and c are evaluated using $\mathbf{S}^{\xi}$.

- η direction,

$$[\mathbf{T}^{\eta}] = \begin{bmatrix} 1 & 0 & 0 & \lambda_4 & \lambda_5 \\ u & \partial x/\partial \zeta & \partial x/\partial \xi & u\lambda_4 + \beta' S_x & u\lambda_5 + \beta' S_x \\ v & \partial y/\partial \zeta & \partial y/\partial \xi & v\lambda_4 + \beta' S_y & v\lambda_5 + \beta' S_y \\ w & \partial z/\partial \zeta & \partial z/\partial \xi & w\lambda_4 + \beta' S_z & w\lambda_5 + \beta' S_z \\ 0 & 0 & 0 & -\lambda_5/\rho & -\lambda_4/\rho \end{bmatrix} \tag{104}$$

$$[\mathbf{T}^{\eta}]^{-1} = \begin{bmatrix} 1 + q^2/\beta' S^2 & -qS_x/\beta' S^2 & -qS_y/\beta' S^2 & -qS_z/\beta' S^2 & -\rho \\ -\mathbf{g}^{\xi} \cdot \mathbf{V}/S^2 & \mathbf{g}^{\xi} \cdot \hat{\imath}/S^2 & \mathbf{g}^{\xi} \cdot \hat{\jmath}/S^2 & \mathbf{g}^{\xi} \cdot \hat{k}/S^2 & 0 \\ \mathbf{g}^{\zeta} \cdot \mathbf{V}/S^2 & -\mathbf{g}^{\zeta} \cdot \hat{\imath}/S^2 & -\mathbf{g}^{\zeta} \cdot \hat{\jmath}/S^2 & -\mathbf{g}^{\zeta} \cdot \hat{k}/S^2 & 0 \\ -q\lambda_4/\beta' S^2 c & \lambda_4 S_x/\beta' S^2 c & \lambda_4 S_y/\beta' S^2 c & \lambda_4 S_z/\beta' S^2 c & \rho/c \\ q\lambda_5/\beta' S^2 c & -\lambda_5 S_x/\beta' S^2 c & -\lambda_5 S_y/\beta' S^2 c & -\lambda_5 S_z/\beta' S^2 c & -\rho/c \end{bmatrix}, \tag{105}$$

where $\mathbf{S}$, q, λ_4, λ_5, and c are evaluated using $\mathbf{S}^{\eta}$.

- ζ direction,

$$[\mathbf{T}^{\zeta}] = \begin{bmatrix} 1 & 0 & 0 & \lambda_4 & \lambda_5 \\ u & \partial x/\partial \xi & \partial x/\partial \eta & u\lambda_4 + \beta' S_x & u\lambda_5 + \beta' S_x \\ v & \partial y/\partial \xi & \partial y/\partial \eta & v\lambda_4 + \beta' S_y & v\lambda_5 + \beta' S_y \\ w & \partial z/\partial \xi & \partial z/\partial \eta & w\lambda_4 + \beta' S_z & w\lambda_5 + \beta' S_z \\ 0 & 0 & 0 & -\lambda_5/\rho & -\lambda_4/\rho \end{bmatrix} \tag{106}$$

$$[\mathbf{T}^{\zeta}]^{-1} = \begin{bmatrix} 1 + q^2/\beta' S^2 & -qS_x/\beta' S^2 & -qS_y/\beta' S^2 & -qS_z/\beta' S^2 & -\rho \\ -\mathbf{g}^{\eta} \cdot \mathbf{V}/S^2 & \mathbf{g}^{\eta} \cdot \hat{\imath}/S^2 & \mathbf{g}^{\eta} \cdot \hat{\jmath}/S^2 & \mathbf{g}^{\eta} \cdot \hat{k}/S^2 & 0 \\ \mathbf{g}^{\xi} \cdot \mathbf{V}/S^2 & -\mathbf{g}^{\xi} \cdot \hat{\imath}/S^2 & -\mathbf{g}^{\xi} \cdot \hat{\jmath}/S^2 & -\mathbf{g}^{\xi} \cdot \hat{k}/S^2 & 0 \\ -q\lambda_4/\beta' S^2 c & \lambda_4 S_x/\beta' S^2 c & \lambda_4 S_y/\beta' S^2 c & \lambda_4 S_z/\beta' S^2 c & \rho/c \\ q\lambda_5/\beta' S^2 c & -\lambda_5 S_x/\beta' S^2 c & -\lambda_5 S_y/\beta' S^2 c & -\lambda_5 S_z/\beta' S^2 c & -\rho/c \end{bmatrix}, \quad (107)$$

where $\mathbf{S}$, q, λ_4, λ_5, and c are evaluated using $\mathbf{S}^{\zeta}$.

ACKNOWLEDGMENTS

The authors thank the Air Force Office of Scientific Research for their support of this research under Grant AFOSR-0403.

REFERENCES

1. H. N. Abramson, *The Dynamic Behavior of Liquids in Moving Containers*, NASA SP-106 (1966).
2. S. N. Antontsev, A. V. Kazhikhov, and V. N. Monakhov, *Boundary Value Problems in Mechanics of Nonhomogeneous Fluids* (North-Holland, Amsterdam, 1990).
3. T. J. Barth, Analysis of implicit local linearization techniques for upwind and TVD algorithms, AIAA Paper 87-0595 (1987).
4. R. Beam and R. F. Warming, *J. Comput. Phys.* **22,** 87 (1976).
5. J. U. Brackbill, D. B. Kothe, and C. Zemach, *J. Comput. Phys.* **100,** 335 (1992).
6. S. Chandrasekhar, *Hydrodynamics and Hydromagnetic Stability* (Clarendon Press, Oxford, 1961).
7. A. J. Chorin, A numerical method for solving incompressible viscous flow problems, *J. Comput. Phys.* **2,** 12 (1967).
8. R. M. Cooper, Dynamics of liquids in moving containers, *Ars J.* **30,** 725 (1960).
9. B. J. Daly, Dynamics of liquids in moving containers, *Phys. Fluids* **10,** 297 (1967).
10. D. A. Edwards, B. Howard, and D. T. Wasan, *Interfacial Transport Processes and Rheology*, (Butterworth–Heinemann, Boston, 1991).
11. F. H. Harlow and J. E. Welch, Numerical study of large-amplitude free-surface motions, *Phys. Fluids* **8,** 2182 (1965).
12. C. Hirsch, *Numerical Computation of Internal and External Flows,* Vol. 2 (Wiley, New York, 1990).
13. C. W. Hirt, J. L. Cook, and T. D. Butler, A Lagrangian method for calculating the dynamics of an incompressible fluid with free surface, *J. Comput. Phys.* **5,** 103 (1970).
14. C. W. Hirt and B. D. Nichols, Volume of fluid (VOF) method for the dynamics of free boundaries, *J. Comput. Phys.* **39,** 201 (1981).
15. A. Jameson and E. Turkel, Implicit schemes and LU decompositions, *Math. Comput.* **37,** 385 (1981).
16. A. Jameson and S. Yoon, Lower-upper implicit schemes with multiple grids for the Euler equations, *AIAA J.* **25,** 929 (1987).
17. A. Jeffrey, *Quasilinear Hyperbolic Systems and Waves* (Pitman, London, 1976).
18. L. Jun and D. B. Spalding, Numerical simulation of flows with moving interfaces, *Phys. Chem. Hydrodyn.* **10,** 625 (1988).
19. I. Kataoka, Local instant formulation of two-phase flow, *Int. J. Multiphase Flow* **12,** 745 (1986).
20. F. J. Kelecy, *Numerical Simulation of Two and Three-Dimensional Viscous Free Surface Flows in Partially-Filled Containers Using a Surface Capturing Approach*, Ph.D. thesis, Iowa State University, 1993.

21. B. P. Leonard, A stable and accurate convective modelling procedure based on quadratic upstream interpolation, *Comput. Methods Appl. Mech. Eng.* **19,** 59 (1979).
22. J. C. Martin, and W. J. Moyce, An experimental study of the collapse of liquid columns on a rigid horizontal plane, *Phil. Trans. Royal Soc. of London Ser. A* **244,** 312 (1952).
23. T. T. Maxwell and D. B. Spalding, Numerical modelling of free surface flows, in *Numerical Methods for Transient and Coupled Problems*, edited by R. W. Lewis, E. Hinton, and B. A. Schrefler (Wiley, New York, 1987).
24. D. Pan and H. Lomax, A new approximate LU factorization scheme for the Reynolds-averaged Navier-Stokes equations, *AIAA J.* **26,** 163 (1988).
25. D. Pan and S. Chakravarthy, Unified formulation for incompressible flows, AIAA Paper 89-0122 (1989).
26. J. D. Ramshaw and J. A. Trapp, A numerical technique for low-speed homogeneous two-phase flow with sharp interfaces, *J. Comput. Phys.* **21,** 438 (1976).
27. Lord Rayleigh, ''Investigation of the character of the equilibrium of an incompressible heavy fluid of variable density,'' in *Scientific Papers,* Vol. 2 (University Press, Cambridge, 1900), p. 200.
28. P. L. Roe, Characteristic-based schemes for the Euler equations, *Annu. Rev. Fluid Mech.* **18,** 337 (1986).
29. S. E. Rogers, D. Kwak, and C. Kiris, Numerical solution of the incompressible Navier-Stokes equations for steady-state and time-dependent problems, AIAA-Paper 89-0463 (1989).
30. L. A. Segel, *Mathematics Applied to Continuum Mechanics* (Macmillan, New York, 1977).
31. J. Simon, Nonhomogeneous viscous incompressible fluids: existence of velocity, density, and pressure, *SIAM J. Math. Anal.* **21,** 1093 (1990).
32. D. B. Spalding, *A Method for Computing Steady and Unsteady Flows Possessing Discontinuities of Density*, Report 910/2, CHAM Ltd., 40 High Street, London SW19 5AU, 1974.
33. M. Sussman, P. Smereka, and S. Osher, A level set approach for computing solution to incompressible two-phase flow, *J. Comput. Phys.* **114,** 146 (1994).
34. G. I. Taylor, The instability of liquid surfaces when accelerated in a direction perpendicular to their planes. I, *Proc. R. Soc. London Ser. A* **201,** 192 (1950).
35. G. Tryggvason, Numerical simulations of Rayleigh-Taylor instability, *J. Comput. Phys.* **75,** 253 (1988).
36. S. O. Unverdi and G. Tryggvason, A front tracking method for viscous, incompressible multi-fluid flows, *J. Comput. Phys.* **100,** 25 (1992).
37. B. van Leer, Upwind difference methods for aerodynamic problems governed by the Euler equations, in *Lect. Notes in Math.,* Vol. 22 (Springer-Verlag, Berlin, 1985), p. 327.
38. M. Vinokur, An analysis of finite-difference and finite-volume formulations of conservation laws, *J. Comput. Phys.* **81,** 1 (1989).
39. J. W. Yakota, Diagonally inverted lower-upper factored implicit multigrid scheme for the three-dimensional Navier-Stokes equations, *AIAA J.* **28,** 1642 (1990).
40. H. C. Yee, *A Class of High Resolution Explicit and Implicit Shock-Capturing Schemes,* Lecture Series 1989-04, March 6–10, 1989, van Karman Institute for Fluid Dynamics.
41. D. L. Youngs, Numerical simulation of turbulent mixing by Rayleigh-Taylor instability, *Physica D* **12,** 32 (1984).